Petrogenesis of the early Cretaceous intra-plate basalts from the Western North China Craton: Implications for the origin of the metasomatized cratonic lithospheric mantle

Junjie Zhang[1, 2, 3], Pengyuan Guo[1, 2]*, Pu Sun[1, 2], Yaoling Niu [1, 2, 4, 5], Yuanyuan Xiao[1, 2], Paulo M. Vasconcelos[6]

[1] Key Laboratory of Marine Geology and Environment, Institute of Oceanology, Chinese Academy of Sciences, Qingdao 266071, China

[2] Laboratory for Marine Geology, Qingdao National Laboratory for Marine Science and Technology, Qingdao 266061, China

[3] University of Chinese Academy of Sciences, Beijing 100049, China

[4] Department of Earth Sciences, Durham University, Durham DH1 3LE, UK

[5] School of Earth Science and Resources, China University of Geosciences, Beijing 100083, China

[6] The University of Queensland, School of Earth Sciences, Brisbane, QLD 4072, Australia

*Corresponding authors:

Dr. P.Y. Guo (guopy@qdio.ac.cn)

Current address:

Institute of Oceanology

Chinese Academy of Sciences

Nanhai Road 7

Qingdao, Shandong 266071

China

From: Dr. Pengyuan Guo
Institute of Oceanology
Chinese Academy of Sciences
Qingdao, Shandong 266071, China

To: Lithos

Date: November 03, 2020

Subject: Revised manuscript submission to Lithos for publication

Dear Editor,

Thank you very much for the constructive comments by the reviewers and yourself. We are now submitting our revised manuscript (Manuscript Number: LITHOS8954). In revision, we have considered all the comments. And we hope you and the reviewers agree that the revised version is essentially ready for publication.

Sincerely yours,

Dr. Pengyuan Guo (guopy@qdio.ac.cn)

Tel: +86-15725261166; +86-0532-82893137

Revision notes:

Thanks very much for the constructive comments by the reviewers and editor. In revision, we have considered all the comments. Furthermore, we also adjusted the text structure in section 5.3 slightly and made the language more accurate. We hope the revised version is essentially ready for publication.

Answers to reviewer:

Reviewer #1:

1. [Line 311] Generally, there are two mechanisms for continental crustal recycling into mantle, (1) lower crustal delamination; (2) continental crust subduction. The recycling of terrigenous sediments is caused by oceanic subduction.

Answer: Have changed and please see the details in the revised manuscript.

2. More statements and representative references for crustal recycling by lower crustal delamination and continental crust subduction should be given in the text.

Answer: The brief description and representative references have been added and please see the details in the revised manuscript.

We present new bulk-rock $^{40}Ar/^{39}Ar$ age, major and trace elements and Sr-Nd-Hf isotopic data on the early Cretaceous intra-plate alkali basalts from the Western North China Craton (WNCC) to study the origin of the metasomatized cratonic lithosphere mantle. The age of these basalts is ~116 Ma. These basalts have elevated incompatible element abundance with high $[La/Sm]_N$ (2.80-4.56) and enriched Sr-Nd-Hf isotopic compositions ($^{87}Sr/^{86}Sr_i$ = 0.7062-0.7075, $\varepsilon_{Nd}(t)$ = -6.0 to -13.0 and $\varepsilon_{Hf}(t)$ = -8.3 to -17.4), being similar to the contemporary analogues from the Western North China Craton and Paleozoic kimberlites and mantle xenoliths. The WNCC basalts also show good correlations between $\varepsilon_{Nd}(t)$ and $\varepsilon_{Hf}(t)$, and high $[La/Sm]_N$. All these geochemical observations are consistent with the interpretation that these basalts originated from partial melting of the lithospheric mantle that experienced melt metasomatism. Two types metasomatism melts are required to explain the geochemical characteristics of these rocks. The obvious negative Nb-Ta (compared with K)-Ti and positive Ba-Pb anomalies observed in these basalts further constrain that one of the metasomatic melts was derived from the subducted terrigenous sediment. Furthermore, the overall higher P/Nd, Nb/La and Nb/Th and lower Lu/Hf of basalts in the WNCC suggest that there is also contribution of low-F melts from asthenosphere mantle. Collectively, we suggest that the formation of the metasomatized lithosphere mantle beneath the WNCC is the process of metasomatic reaction between mantle peridotite and the melts of different origin to generate metasomatic veins containing amphibole/phlogopite. Partial melting of the metasomatic lithospheric mantle at 106-120 Ma in the WNCC was considered to be induced by thermal perturbation that was ultimately related to the breakoff of the subducted oceanic slab following the closure of the Mongolia-Okhotsk ocean.

Highlight

1. We report early Cretaceous volcanic rocks in West NCC.

2. The basalts originated from partial melting of metasomatized lithospheric mantle.

3 Metasomatism agents were melts from asthenosphere mantle and subducted sediments.

4. The WNCC magmatism was related to slab breakoff of subducted Mongolia-Okhotsk ocean.

Petrogenesis of the early Cretaceous intra-plate basalts from the Western North China Craton: Implications for the origin of the metasomatized cratonic lithospheric mantle

Junjie Zhang[1, 2, 3], Pengyuan Guo[1, 2]*, Pu Sun[1, 2], Yaoling Niu [1, 2, 4, 5], Yuanyuan Xiao[1, 2], Paulo M. Vasconcelos[6]

[1] Key Laboratory of Marine Geology and Environment, Institute of Oceanology, Chinese Academy of Sciences, Qingdao 266071, China

[2] Laboratory for Marine Geology, Qingdao National Laboratory for Marine Science and Technology, Qingdao 266061, China

[3] University of Chinese Academy of Sciences, Beijing 100049, China

[4] Department of Earth Sciences, Durham University, Durham DH1 3LE, UK

[5] School of Earth Science and Resources, China University of Geosciences, Beijing 100083, China

[6] The University of Queensland, School of Earth Sciences, Brisbane, QLD 4072, Australia

*Corresponding authors:

Dr. P.Y. Guo (guopy@qdio.ac.cn)

Current address:

Institute of Oceanology

Chinese Academy of Sciences

Nanhai Road 7

Qingdao, Shandong 266071

China

Abstract: We present new bulk-rock $^{40}Ar/^{39}Ar$ age, major and trace elements and Sr-Nd-Hf isotopic data on the early Cretaceous intra-plate alkali basalts from the Western North China Craton (WNCC) to study the origin of the metasomatized cratonic lithosphere mantle. The age of these basalts is ~116 Ma. These basalts have elevated incompatible element abundance with high $[La/Sm]_N$ (2.80-4.56) and enriched Sr-Nd-Hf isotopic compositions ($^{87}Sr/^{86}Sr_i$ = 0.7062-0.7075, $\varepsilon_{Nd}(t)$ = -6.0 to -13.0 and $\varepsilon_{Hf}(t)$ = -8.3 to -17.4), being similar to the contemporary analogues from the Western North China Craton and Paleozoic kimberlites and mantle xenoliths. The WNCC basalts also show good correlations between $\varepsilon_{Nd}(t)$ and $\varepsilon_{Hf}(t)$, and high $[La/Sm]_N$. All these geochemical observations are consistent with the interpretation that these basalts originated from partial melting of the lithospheric mantle that experienced melt metasomatism. Two types metasomatism melts are required to explain the geochemical characteristics of these rocks. The obvious negative Nb-Ta (compared with K)-Ti and positive Ba-Pb anomalies observed in these basalts further constrain that one of the metasomatic melts was derived from the subducted terrigenous sediment. Furthermore, the overall higher P/Nd, Nb/La and Nb/Th and lower Lu/Hf of basalts in the WNCC suggest that there is also contribution of low-F melts from asthenosphere mantle. Collectively, we suggest that the formation of the metasomatized lithosphere mantle beneath the WNCC is the process of metasomatic reaction between mantle peridotite and the melts of different origin to generate metasomatic veins containing amphibole/phlogopite. Partial melting of the metasomatic lithospheric mantle at 106-120 Ma in the WNCC was considered to be induced by thermal perturbation that was ultimately related to the breakoff of the subducted oceanic slab following the closure of the Mongolia-Okhotsk ocean.

Keywords: Western North China Craton, K-rich basalt, mantle metasomatism, craton metasomatized lithosphere, subducted terrigenous sediments, Low-F melt

1. Introduction

Cratonic lithospheric mantle is physically thick, cold, buoyant and rigid and geochemically depleted in incompatible element with high MgO and low FeO, which is thought to be the residue of the upper mantle after high extent of melt extraction in early history of the earth (e.g., Abbot et al., 1997; Jordan, 1988; Ringwood, 1975). For this reason, the overlying continental crust can survive for a long time. However, the processes of lateral subduction (e.g., Hawkesworth, 1993) and vertical upwelling of melts/fluids from the asthenospheric mantle (e.g., Niu, 2005, 2014) could potentially change the mineralogy and geochemistry of the cratonic lithosphere mantle, resulting in varying extents of lithosphere modification/re-fertilization and increasing the susceptibility of the craton destruction/lithosphere thinning. Therefore, the melts or xenoliths derived from such ancient metasomatized cratonic lithosphere mantle, for example, the North China Craton (NCC), would contain important information on the cratonic lithosphere re-fertilization history.

Previous studies, mostly based on ＞110 Ma mafic igneous rocks in the Eastern North China Craton (ENCC), showed that the partial melts derived from the metasomatized NCC lithospheric mantle share the similar continental crust-like signatures of being enriched in large ion lithosphere elements (LILE; e.g., Rb, Ba, K), depleted in high field strength elements (HFSE; e.g., Nb, Ta, Ti) and with enriched Sr-Nd-Hf isotope compositions (radiogenic Sr and unradiogenic Nd-Hf) (e.g., Dai et al., 2016; Liu et al., 2008; Meng et al., 2015), implying that the whole NCC lithospheric mantle experienced re-fertilization before partial melting. Formation of the enriched lithosphere mantle of NCC has been ascribed to: (1) the delamination of the lower continental crust (e.g., Gao et al., 2004, 2008; Liu et al., 2008); (2) the subduction of continental crust of South China Block (e.g., Dai et al., 2016; Yang et al., 2012; Zhang et al., 2002; Zhao et al., 2018); (3) the subduction of the Paleo-Pacific plate (e.g., Ma et al.,

2014). The “delamination of lower crust” model deciphers the scenario that the lithosphere mantle was enriched/metasomatized by the melts derived from foundered lower crust (Gao et al., 2004, 2008; Liu et al., 2008). While this model is attractive, it is physically not straightforward how the lower continental crust of the NCC together with buoyant lithospheric mantle foundered into the asthenosphere mantle in scale of the whole North China (Niu, 2014). Furthermore, the thickening of the lower crust is the prerequisite for the crust delamination. But except for some areas (e.g., Xuhuai), there is no enough evidence to show that this process occurred in the whole North China Craton (Wu et al., 2008 and references therein). The “continent-continent subduction/collision” model means the lithosphere mantle enriched through interaction with melt generated from melting of the subducted crust of South China Block (Dai et al., 2016; Yang et al., 2012; Zhang et al., 2002; Zhao et al., 2018). This model cannot explain the origin of the enriched lithospheric mantle beneath the north margin and interior of the NCC, but only works restricted to the areas close to the Dabie–Sulu Orogenic Belt. Some studies suggest the lithosphere mantle was modified by subduction-related fluids from Paleo-Pacific plate (e.g., Ma et al., 2014). Similarly, the subduction of the Paleo-Pacific plate modal cannot explain the origin of the enriched lithospheric mantle beneath the area far from the Pacific subduction zone, for example, the Western North China Craton (WNCC).

There is growing evidence that the lithosphere under WNCC has also been thinning in the Mesozoic (Chen et al., 2009; Guo et al., 2014) as evidenced by the widespread late Cretaceous volcanic rocks along north margin of WNCC (Fig. 1a; Guo et al., 2014, 2018; He et al., 2013; Zhang, 2013; Zhong et al., 2014, 2015; Zou et al., 2008). These early Cretaceous basalts have high incompatible element abundances and highly enriched Sr-Nd-Hf isotopic compositions (e.g., Guo et al., 2014, 2018; Zhong et al., 2014, 2015), implying they also originated from an ancient metasomatized lithosphere mantle (Guo

et al., 2014, 2018). However, the mechanism of the enriched mantle formation was unclear in details. The study of lithosphere mantle enrichment beneath northern margin of WNCC could help us to understand the mantle re-fertilization beneath the area far from Dabie–Sulu Orogenic Belt and Pacific subduction zone and have a significant meaning in the exploration of the evolution of whole NCC.

Here we present new bulk-rock $^{40}Ar/^{39}Ar$ dating, major element, trace element and Sr-Nd-Hf isotopic data on the early Cretaceous basalts from Wulate Zhongqi and Heishitougou, Western North China Craton (WNCC; Fig. 1) to study the origin of the metasomatized lithospheric mantle beneath WNCC. The data suggest that the enriched lithospheric mantle beneath the WNCC was formed through metasomatism by silicate melts derived from terrigenous sediments and low-F melts from asthenosphere mantle. These processes could lead to the formation of metasomatic dikes/veins containing amphibolite/phlogopite. Integrated with the regional geology, we suggest that the sediments were recycled into the mantle depth together with the subducted Paleo-Asia ocean slab in early Paleozoic, while subsequent melting of the metasomatized lithospheric mantle materials in early Cretaceous produced the WNCC intra-plate alkali basalts.

2. Geological setting and samples

The North China Craton is one of the oldest cratons on the earth with the history in excess of 3.8 Gyrs (e.g., Liu et al., 1992). It is bounded by the Central Asian Orogenic Belt (CAOB) to the north and the Qinling-Dabie-Sulu high-ultrahigh pressure metamorphic belt to the south (Fig.1a). It can be divided into Eastern North China Craton (ENCC) and Western North China Craton (WNCC) based on the studies of the basement rocks (Fig. 1a; e.g., Zhao et al., 2001). The WNCC is further divided into the Yinshan block in the north and the Ordos block in the south by the nearly E-W trending, ca. 2.0 to 1.9 Ga Khondalite Belt (Zhao et al., 2005). After the amalgamation of the eastern and western blocks, the North

China Craton remained tectono-thermally quiescent until the Mesozoic. Previous studies showed that the ENCC experienced extensive destruction/lithosphere thinning in the Mesozoic (> ~110 Ma) (Niu, 2005, 2014; Zhu et al., 2011), while the lithosphere thinning in the WNCC was limited in the northern margin (Chen et al., 2009; Guo et al., 2014).

The northern margin of the WNCC was an active continental margin during Paleozoic to Early Triassic with the Paleo-Asian slab subducting southward (Li, 2006; Xiao et al., 2003; Zhang et al., 2009). The Paleo-Asian ocean closed in early Triassic when the North China Craton collided with the southern Mongolian composite terrane along the Solonker Suture (SLS; Wilde, 2015). Following the closure of the Paleo-Asian ocean, the northern margin of the NCC became active continental margin again with the Mongolia-Okhotsk Ocean subducting southward. The Mongolia-Okhotsk Ocean was ultimately closed in Jurassic to the earliest Cretaceous (Donskaya et al., 2013; Tomurtogoo et al., 2005), and the region came into intra-plate tectonic setting in early Cretaceous. So far, only several outcrops of Early Cretaceous volcanic rocks have been reported in the WNCC, i.e., Siziwang Qi, Wuchuan Basin, Guyang Basin, Wulate Houqi and Suhongtu, dominated by mafic-intermedium compositions with minor felsic volcanic assemblages (Fig. 1a; Guo et al., 2014, 2018; He et al., 2013; Zhang, 2013; Zhong et al., 2014, 2015; Zou et al., 2008). These volcanic rocks were erupted during 135~105 Ma and are spatially distributed along the northern margin of the WNCC (Table 1 and Fig.1a), forming an E-W trending volcanic rock belt.

Wulate Zhongqi is a newly identified Mesozoic volcanism outcrop that is located on the north margin of the WNCC (Fig. 1). These basalts, erupted on the Cretaceous red sedimental layer (Fig. 2a), covers a large area of ~240 km^2 (Fig. 1b). Heishitougou is located ~150 km south of the Wulate Zhongqi in Khondalite Belt (Fig. 1). Heishitougou volcanic rocks are covered under the Quaternary sediments

with very limited outcrops of 2-3 meters thick (Fig. 2b) and their eruption age is 126.2 Ma (Zou et al., 2008). The samples in this study include Wulate Zhongqi basalts and andesitic basalts and Heishitougou basalts. Most basalt and andesitic basalt samples are massive with intergranular texture, being made up of microlites of plagioclase, olivine, clinopyroxene and magnetite (Fig. 2c, d, f). Several Wulate Zhongqi samples have porphyritic texture with olivine (~5-10%) and plagioclase (~5%) as phenocrysts, and most of olivine phenocrysts were altered into iddingsite (Fig. 2e). Their groundmass, with intergranular texture, is made up of microlites of plagioclase, clinopyroxene and olivine (Fig. 2e).

3. Sample preparation and analytical procedure

3.1 ^{40}Ar-^{39}Ar Geochronology

We selected the freshest basaltic sample (ZQ14-47; Fig. 2f) for ^{40}Ar-^{39}Ar dating. The sample grains were irradiated for 14 hours in the Cadmium-lined B-1 CLICIT facility, a TRIGA-type reactor, in Oregon State University, USA. After a decay period of irradiation, samples were analysed by laser ^{40}Ar/^{39}Ar heating following procedures detailed in Vasconcelos et al. (2002). Before analysis, the rock grains and fluence monitors were baked-out under vacuum at ~200 ℃ for ~12 hours. The sample was heated incrementally with a continuous-wave Verdi Diode laser (532 nm) with a 2 mm wide defocused beam. The fraction of gas released was cleaned through a cryocooled cold-trap (T = -125 ℃) and two C-50 SAES Zr-V-Fe getters and analysed for Ar isotopes in a MAP215-50 mass spectrometer equipped with a third C-50 SAES Zr-V-Fe getter. Analytical procedures followed are described in Deino and Potts (1990) and Vasconcelos et al. (2002). A ^{40}Ar/^{36}Ar value of 298.56 ± 0.31 for atmospheric argon was used for the calculation of the mass spectrometer discrimination (Renne et al., 2009). The irradiation correction factor (J) for each Al-disk were determined by the laser total fusion analyses of 15 individual aliquots of neutron fluence monitor.

158 **3.2 Geochemistry**

159 Eighteen samples were chosen for geochemical analyses. We removed weathered surfaces, pen
160 marks and saw marks first. All samples were crushed into grains of ~0.5-1.0 mm size to painstakingly
161 remove phenocrysts under a binocular. The sample grains were then ultrasonically-cleaned with Milli-Q
162 water and dried in a clean environment before analyses.

163 All the bulk-rock geochemical analyses were done at the Laboratory of Ocean Lithosphere and
164 Mantle Geodynamic, Institute of Oceanology, Chinese Academy of Sciences. Major elements were
165 analyzed using an Agilent 5100 inductively coupled plasma-optical emission spectroscopy (ICP-OES)
166 following Kong et al. (2019). After dried at 105 ℃ for ~2 hours in the oven, about ~50 mg rock powders
167 were weighted in platinum crucibles together with ~250 mg lithium metaborate. The platinum crucibles
168 were heated in the muffle furnace at 1050 ℃ for 2 hours until the mixture completely molten. The crucible
169 was further heated over a Bunsen burner (Dragon series) at 1000 ℃ and stirred to ensure all sample
170 materials forming a single coherent melt drop that was finally poured/quenched and resolved in 5%
171 HNO_3 at room temperature. USGS standards materials BCR-2 and AGV-2 were used to monitor the
172 analytical accuracy and precision. For loss on ignition (LOI) analysis, ~500 mg samples were weighed
173 and heated in a muffle furnace at 1000 ℃ for 30 min, cooled in a desiccator, and then weighed again to
174 calculate the weight loss as the LOI (see Supplementary Table 1).

175 Trace elements were analyzed using an Agilent-7900 inductively coupled plasma mass
176 spectrometer (ICP-MS) following Chen et al. (2017). About 50 mg rock powders were dissolved with
177 distilled HNO_3+ HCl+ HF in a high-pressure jacket equipped Teflon beaker at 190 °C for 15 hours. The
178 sample solutions are then evaporated to incipient dryness at 100 ℃, refluxed with 2 ml of concentrated
179 HNO_3 before being heated again to incipient dryness to remove all the residual HF, and then re-dissolved

with distilled 20% HNO_3 for 2 hours till complete digestion/dissolution. USGS standards materials BCR-2 and AGV-2 were used to monitor the analytical accuracy and precision (see Supplementary Table 1).

The Sr-Nd-Hf isotope ratios were measured using a Nu Plasma II Multi-Collector Inductively Coupled Plasma Mass Spectrometer (MC ICP-MS) following the procedures of Sun et al. (2019). The sample dissolving process was similar to that for trace elements analysis, and the final solution was re-dissolved in 2 ml 3N HNO_3. The final sample solution was first loaded onto Sr-spec resin columns to separate Sr with the eluted sample solution collected and then loaded onto AG 50W-X8 resin columns to separate REE. The eluted sample solution from AG 50W-X8 resin columns was collected and then loaded onto Ln-spec resin columns to collect Hf. The separated REE solution was dried and re-dissolved with 0.25 N HCl before being loaded onto Ln-spec resin columns to collect Nd. The measured $^{87}Sr/^{86}Sr$, $^{143}Nd/^{144}Nd$, and $^{176}Hf/^{177}Hf$ isotope ratios were normalized for instrumental mass fraction using the exponential law to $^{86}Sr/^{88}Sr = 0.1194$, $^{146}Nd/^{144}Nd = 0.7219$ and $^{179}Hf/^{177}Hf = 0.7325$, respectively. Standards of NBS-987, JNdi-1 and Alfa Hf were analyzed every three to five samples to monitor the instrument drift for Sr, Nd and Hf isotopes, respectively. Repeated analysis for NBS-987 gave an average $^{87}Sr/^{86}Sr = 0.710251 \pm 0.000020$ (n=8, 2σ), for JNdi-1 gave an average $^{143}Nd/^{144}Nd = 0.512111 \pm 0.000003$, (n=6, 2σ), and for Alfa Hf gave an average $^{176}Hf/^{177}Hf = 0.282196 \pm 0.000007$ (n=8, 2σ). The analysis results of USGS reference materials AGV-2, BCR-2 and BHVO-2 run with our samples are given in Table 2, which are all consistent with the reported reference values (GeoREM, http://georem.mpch-mainz.gwdg.de/).

4. Results

4.1 ^{40}Ar-^{39}Ar geochronological data

The ^{40}Ar-^{39}Ar age data for sample ZQ14-47 from Wulate Zhongqi is reported in Supplementary

Table 2 and shown in Fig. 3. The sample was analysed twice, and the two incremental heating spectra of sample ZQ14-47 define similar plateau-like segments, containing ~40 and 50% of the total ^{39}Ar released, and these plateau-like segments yield compatible ages of 119.65 ± 0.40 and 119.54 ± 0.53 Ma (Fig. 3a). An integrated apparent age obtained by combining the results from all steps analysed is also shown (Fig. 3b). Inverse isochron was gotten by plotting all results on a $^{39}Ar/^{40}Ar$ vs. $^{36}Ar/^{40}Ar$ diagram and the inverse age was calculated from the $^{39}Ar/^{40}Ar$ intercept of isochron on the diagram. However, the inverse isochron suggests significant excess argon in the sample ($^{40}Ar/^{36}Ar$ intercept = 857 ± 72). In this case, the inverse isochron is more reliable here and the calculated inverse isochron age is 116.35 ± 0.75 Ma. Therefore, the age of these basalts is ~116 Ma.

4.2 Geochemical data

Major and trace element data on our WNCC basalt samples are given in Supplementary Table 1. These samples have high alkali content ($Na_2O + K_2O$ = 4.81- 7.78 wt.%), and they are trachybasalts, basaltic trachyte-andesite and trachyandesite according to Le Bas et al. (1986) (Fig. S1a) and belong to shoshonite and high-K series according to Le Maitre et al. (1989) (Fig. S1b). For simplicity, these samples are hereafter referred to as basalt. Volcanic rocks from Wulate Zhongqi display a relative larger compositional variation (Fig. 4 & S1). Samples from Wulate Zhonqi show increasing SiO_2, Al_2O_3 and TiO_2 and decreasing $^{T}Fe_2O_3$, CaO/Al_2O_3, Cr and Ni with decreasing MgO (Fig. 4). The Heishitougou samples have a uniform composition with higher TiO_2, $^{T}Fe_2O_3$, and lower SiO_2 at a given MgO when compared with the Wulate Zhongqi samples (Fig. 4).

In chondrite-normalized rare earth element (REE) diagram (Fig. 5a), the WNCC samples show consistent enrichment in light rare earth elements (LREEs) and depletion in heavy rare earth elements (HREEs) ($[La/Sm]_N$ = 2.80-4.56) without obvious Eu negative anomaly, being similar to the >110 Ma

basaltic rocks in ENCC (Dai et al., 2016; Liu et al., 2008). In primitive mantle normalized multi-element spidergram (Fig. 5b), these samples display positive Ba and Pb anomalies and negative Ti anomalies. Different from the analogues in the ENCC (Dai et al., 2016; Liu et al., 2008), basalts from WNCC have higher Nb-Ta-Ti abundances and thus show less obvious Nb-Ta trough, implying somewhat different mantle source or source history.

Bulk-rock Sr, Nd and Hf isotopic data of our WNCC samples are given in Table 2. The initial Sr-Nd-Hf isotope ratios were calculated using the age of 116.35 Ma (this study) and 126.2 Ma (Zou et al., 2008) for samples from Wulate Zhongqi and Heishitougou, respectively. Generally, these samples show enriched isotopic compositions with a large range of $^{87}Sr/^{86}Sr_i$ = 0.7062-0.7075, $\varepsilon_{Nd}(t)$ = -6.0 to -13.0 and $\varepsilon_{Hf}(t)$ = -8.3 to -17.4, plotting in the field defined by the >110 Ma basaltic rocks from the ENCC in both Sr-Nd and Hf-Nd isotopes spaces (Fig. 6).

5. Discussions

5.1 Evaluation of post-magmatic processes

The samples in this study have been altered to some extent based on the petrographic observation (Fig. 2c-e) and high LOI (>2.5%) in 8 samples (Supplementary Table 1). However, our samples show good correlations between "alteration immobile" elements (e.g., Zr) and most other elements (e.g., Ba, Pb, La, Hf) (Fig. S2), implying that most elements are not influenced by such slight alteration and only Rb was affected in some samples. For these reasons, the following discussion will not involve the elements affected by alteration (e.g., Rb), but use those more immobile elements such as Th, REE, HFSE.

The Wulate Zhongqi samples have relatively large SiO_2 variation (50.71-57.32 wt.%) with low MgO (1.58-5.45 wt.%), Ni (16-55 ppm) and Cr (26-102 ppm) concentration, indicating their evolved nature from mantle-derived parental melts through fractional crystallization. The correlated variations between

246 $^{T}Fe_2O_3$, CaO/Al_2O_3, Ni, Cr and MgO (Fig. 4) indicate the olivine and clinopyroxene as the dominant
247 fractional crystallization phases, being consistent with the petrographic observation. Furthermore, the
248 negative correlation between Al_2O_3 and MgO (Fig. 4c) and no obvious Eu negative anomalies (Fig. 5a)
249 suggest that plagioclase was not the dominant fractional crystallization phase.

250 Crustal contamination is inevitable for mantle-derived melts during their ascent through the thick
251 continental crust. Thus, it is necessary to evaluate the effect of crustal contamination before using the
252 geochemical data to discuss their source characters and mantle melting processes. The continental crust
253 is characterized by elevated abundances of SiO_2 and LILEs and depletion in HFSEs with low $^{143}Nd/^{144}Nd$
254 (Gao et al., 1998; Liu et al., 2004). If a significant volume of crustal materials was involved, there must
255 be an obvious positive relationship between SiO_2/MgO, Nb/La and $\varepsilon_{Hf}(t)$ (or $\varepsilon_{Nd}(t)$). The rough
256 correlations between $\varepsilon_{Hf}(t)$ and these element ratios are found in four samples (ZQ14-09, ZQ14-26,
257 ZQ14-52, ZQ19-08), indicating that they had undergone various levels of crustal assimilation (Fig. 7).
258 However, for most samples, crustal contamination is limited (Fig. 7). Thus, the characteristics of these
259 samples, excluding ZQ14-09, ZQ14-26, ZQ14-52 and ZQ19-08, could reflect those of the magma source,
260 and the four samples potentially contaminated by the crustal materials would not be covered in the
261 following discussion.

262 **5.2 Melt metasomatized lithospheric mantle source of the WNCC basalts**

263 Previous studies explain the widespread >110 Ma intra-plate alkali basalt with high $^{87}Sr/^{86}Sr$, low
264 $^{143}Nd/^{144}Nd$ and low $^{176}Hf/^{177}Hf$ in the ENCC (Fig. 6; Dai et al., 2016; Meng et al., 2015) as the partial
265 melts of the metasomatized cratonic lithosphere (e.g., Meng et al., 2015; Niu, 2005, 2014). This is easily
266 understood. As the cratonic lithospheric mantle is isolated from the underlying convective mantle, it
267 tends to inherit the enriched isotopic compositions of metasomatic agents once the mantle was

metasomatized by isotopically enriched melts or tends to accumulate radiogenic isotopes with time if the mantle was metasomatized by melts with high parent/daughter ratios. The basalts from the Wulate Zhongqi and Heishitougou show significantly radiogenic Sr and un-radiogenic Nd-Hf isotopic compositions, being distinctly different from the asthenospheric mantle derived mid-ocean ridge basalts (MORB) but plotted in the region defined by the >110 Ma basalts from ENCC and basalts with similar age from WNCC in Sr-Nd and Nd-Hf isotopes spaces (Fig. 6). This implies that basalts from Wulate Zhongqi and Heishitougou shared similar origin from partial melting of the lithospheric mantle with these ENCC and WNCC basalts. Importantly, in Sr-Nd isotope space, these basalts also plot in the field of NCC ancient lithosphere mantle represented by Paleozoic kimberlites and mantle xenoliths from NCC (Fig. 6a), providing evidence that the source of these basalts is lithosphere mantle.

Theoretically, the craton lithospheric mantle is the partial melting residues, refractory and highly depleted in incompatible elements (Abbot et al., 1997; Jordan, 1988; Ringwood, 1975). However, this is inconsistent with the basic observation that the occurrence of large scale of the Mesozoic volcanism (Zhu et al., 2011) and incompatible elements highly enriched magmas derived from such a craton lithospheric mantle (e.g., Dai et al., 2016; Liu et al., 2008). This implies that the enrichment or re-fertilization process/processes occurred at the mantle lithosphere before its melting. The WNCC basalts display remarkably enrichment in incompatible elements with high $[La/Sm]_N$ = 2.80-4.56 (Fig. 5), indicating that their mantle source was enriched by melts. Specifically, the significantly correlated $\varepsilon_{Nd}(t)$ with $\varepsilon_{Hf}(t)$ (R= 0.968) in these samples (excluding the sample ZQ14-29) is consistent with that the mantle source isotopic variation is largely controlled by simple magmatic processes. All these geochemical observations imply that the mantle source of the WNCC basalts was the craton lithospheric mantle that was metasomatized by melts.

5.3 The origin of the metasomatic melt and the formation of enriched lithosphere mantle

WNCC basalts display obviously different incompatible element distribution pattern from present-day average OIB with negative Nb-Ta (compared with K) -Ti and positive Ba-Pb anomalies (Fig. 5). Several processes can be responsible for the negative Nb-Ta (compared with K) and Ti anomalies in these samples (Fig. 5): (1) the involvement of the continental crust materials during the magma ascent; (2) Ti-rich mineral (e.g., amphibole, rutile) crystallization during the magma evolution or being as a residual phase in the source region (e.g., Tiepolo et al., 2001; Xiong et al., 2005); (3) Contribution of crustal component in the mantle source (e.g., Cheng et al., 2018; Dai et al., 2016; Liu et al., 2008). First, as discussed above, continental crustal contamination was negligible in the petrogenesis of our samples. Second, TiO_2 increases with the decreasing MgO in our samples (Fig. 4d), arguing against the Ti-bearing minerals crystal fractionation. Furthermore, the fractional crystallization of Ti-bearing minerals or their being as a residual phase in the source region could not produce the Pb anomaly as observed in our samples (Fig. 5b). Therefore, the involvement of crustal materials was the most probable cause to the Nb-Ta-Ti and positive Pb-Ba anomalies in the mantle source of these basalts (Fig. 5b).

Three mechanisms have been proposed to produce continental crustal material recycling into mantle: (1) lower crustal delamination (e.g., Gao et al., 2004, 2008; Liu et al., 2008); (2) continental crust subduction (e.g., Dai et al., 2016; Yang et al., 2012; Zhang et al., 2002; Zhao et al., 2018); (3) sediments recycling by oceanic subduction (e.g., Cheng et al., 2018; Sun et al., 2019). Zhang et al. (2012) suggested that the lithosphere mantle beneath WNCC was not newly-accreted in the Phanerozoic but was transformed from the Archean-Proterozoic lithospheric mantle. Considering the existence of ancient lithospheric relicts in the lithosphere mantle beneath the WNCC, the possibility of lower crust with lithosphere mantle foundering (delamination) into the denser asthenosphere could be excluded.

312 Furthermore, there is no evidence of continental crust subduction in the study area just as the case of
313 South China block subduction underneath the southern margin of the NCC. We therefore suggest the
314 continental crust materials presenting in the mantle source region was most likely originated from
315 subducted sediments. This inference is also consistent with the research of Tertiary basalts-hosted
316 xenoliths from north margin NCC (Wang et al., 2019). Subduction sediments consist of terrigenous
317 sediments and pelagic sediments. Considering that most trace elements (e.g., alkali elements, HFSEs,
318 REEs) of subduction sediments are mainly linked to terrigenous sediments (Plank and Langmuir, 1998),
319 we suggest the crust-like geochemical characters of basalts in this study are the results of involvement
320 of terrigenous sediments in the mantle source. Because the subducted terrigenous sediments is
321 characterized by depletion in HFSEs and P and enriched Sr-Nd-Hf isotope composition (Plank and
322 Langmuir, 1998), the contribution of terrigenous sediment material into the mantle source would
323 decrease P/Nd, Nb/La, $\varepsilon_{Nd}(t)$ and $\varepsilon_{Hf}(t)$ in the erupting magma. This is indeed the case for the WNCC
324 basalts, with both $\varepsilon_{Nd}(t)$ and $\varepsilon_{Hf}(t)$ showing positive correlation with P/Nd and Nb/La (Fig. 8a-d).
325 Therefore, the silica-rich melts derived from subducted terrigenous sediments is an important
326 metasomatism agent beneath WNCC.

327 However, the mantle source only metasomatized by silica-rich melts derived from subducted
328 sediment is not consistent with the geochemical trends of WNCC basalts (Fig. 8), which requires another
329 enriched component in the mantle source. This component must have higher Nb/La and P/Nd, lower
330 Sm/Nd and Lu/Hf than N-MORB and moderately low $\varepsilon_{Nd}(t)$ and $\varepsilon_{Hf}(t)$ (Fig. 8), which implies that this
331 component is characterized by enrichment of incompatible elements and more enrichment in the
332 progressively more incompatible elements. The most likely candidate for this enriched component is the
333 low mass fraction (low-F) melts (Niu and O'Hara, 2003; Niu et al., 2012). Niu and coauthors suggest

such low-F melts may develop within asthenosphere/LVZ and is enriched in volatiles, alkalis and incompatible elements, and it will develop low $\varepsilon_{Nd}(t)$ and $\varepsilon_{Hf}(t)$ after long-term accumulation of radioisotopes, because of its low Sm/Nd and Lu/Hf (Niu and O'Hara, 2003; Niu et al., 2012). They also proposed that OIB was originated from such low-F melts metasomatized mantle (Niu and O'Hara, 2003; Niu et al., 2012). The occurrence of the Early Cretaceous basalts with OIB-like trace elements patterns from Suhongtu and Siziwangqi in the WNCC (Guo et al., 2014; Hui et al., 2020) suggests that low-F melts metasomatism process is common in the lithosphere mantle beneath the region. Note that the WNCC lavas display a contrasting difference from the contemporary analogues in ENCC with obvious Th-U negative anomalies relative to Nb-Ta (Fig. 5b). We explain this observation as the result of the involvement of phlogopite/amphibole metasomes during magma event that produce WNCC lavas. This is because reaction between low-F melts from asthenosphere and Si-poor peridotites could produce phlogopite/amphibole metasomes (Niu, 2008; Pilet et al., 2011; Soder et al., 2016) and partial melts derived from the phlogopite/amphibole -bearing mantle could inherit their mantle source low Th-U and elevated Nb-Ta characters (Pilet et al., 2008).

To illustrate the two metasomatic melts roles in the formation of the metasomatic lithospheric mantle source of the WNCC Mesozoic basalts, we approximate basalts from Siziwangqi as the result of partial melts derived from low-F melts metasomatized mantle (Guo et al., 2014) and choose global subducted sediments (GLOSS, Plank and Langmuir, 1998) as the end-members of subducted terrigenous sediments to model its contribution. The modeling result shows that ~40% terrigenous sediments are required to mix with the Siziwangqi highly enriched basaltic melts to produce the Wulate Zhongqi and Heishitougou lavas (Fig. 9). Not that the modelling result is not unique, which depends on end-members and parameters we chose. However, what we emphasis here is that there are two different metasomatized

agents in the WNCC basalts mantle source.

In conclusion, despite the possible varied compositions of the initial metasomatism melts (derived from subducted sediments or asthenosphere) and the complex reaction between the melts and the peridotite matrix, the ultimate result of such a metasomatism is the formation of the metasomes characterized by an assemblage of hydrous and anhydrous metasomatic minerals such as pyroxene, amphibole and/or phlogopite (Förster et al., 2019; Niu, 2008; Pilet et al., 2011; Sekine and Wyllie, 1983; Soder et al., 2016; Wyllie and Sekine, 1982). Partial melting of such metasomatized mantle produced K-enriched and shoshonitic WNCC basalts, and these basalts inherited the geochemical characters of terrigenous sediments and low-F melts from asthenosphere with enrichment in incompatible elements, obvious Nb-Ta (compared with K)-Ti negative anomalies, Ba-Pb positive anomalies and Th-U trough (Fig. 5b).

5.4 A petrogenetic model for the generation of widespread WNCC basalts

Because the study area is located at the northern margin of the NCC, the first and foremost tectonic background related to these magmatism activities is the closure of the Paleo-Asian ocean. However, the Paleo-Asian ocean was closed in late Permian to early Triassic (Li, 2006; Xiao et al., 2003; Zhang et al., 2009). The temporal span from such an event to the early Cretaceous magmatism is at least ~100 Myrs, which makes it impossible to be related with each other. In addition, as there is no known regional domal uplift nor the presence of volumetrically significant “large igneous province”, the WNCC volcanisms are unlikely to have been caused by a hotspot or mantle plume. Third, the addition of fluids, released from the speculated Paleo-Pacific slabs lying in the transition zone, to the ancient craton lithosphere could well explain the >110 Ma basaltic magmatism in the ENCC (Niu, 2005, 2014). But this mechanism may not apply here because the WNCC is too far (~1500 km) away from the speculated western pacific

subduction zone. Thus, other mechanism is required to explain the petrogenesis of these intra-plate basalts.

Previous studies demonstrate that extensional basins (e.g., Graham et al., 2001) and metamorphic core complexes (e.g., Davis et al., 2002) of early Cretaceous ages are widespread in the northern margin of the WNCC, suggesting an extensional setting at that time in the region. Some authors explained such an extension to be related with the breakoff of subducted oceanic slab after the closure of Mongolia-Okhotsk Ocean in the Middle Jurassic (Li et al., 2018; Ouyang et al., 2015). Our contemporary basaltic volcanism in WNCC supports this model. We also suggest that the early Cretaceous basaltic volcanism in the WNCC in this study and in other recent literature (Table 1; Fig. 1; Guo et al., 2014, 2018; He et al., 2013; Zhang, 2013; Zhong et al., 2014, 2015; Zou et al., 2008) were all the products of the same tectonic-thermal event.

As discussed above, the mantle source of WNCC basalts have underwent metasomatism by melts from subducted terrigenous sediments. The subduction of both Paleo-Asian oceanic slab and Mongolia-Okhotsk seafloor slab could bring the sediments into mantle. However, given that the Tertiary basalt-hosting mantle xenoliths from northern margin of NCC have the character of metasomatism by melts of Paleo-Asian Ocean sediments (Wang et al., 2019) and the north margin of the WNCC is closed to the Solonker suture spatially. We preferred that the Paleo-Asian Ocean subducted sediment is more prior to affect the NCC lithospheric mantle.

Following this interpretation, we propose a petrogenic model for the WNCC basalts as follows. In the Paleozoic, the Paleo-Asian oceanic slab subducted underneath the North China Craton (Li, 2006; Xiao et al., 2003; Zhang et al., 2009), carrying continent-derived sediments (Fig. 10a). Melts derived from these subducted sediments metasomatized the base of the lithosphere mantle beneath the northern

margin of the WNCC and formed the metasomatic veins (Wang et al., 2019; Fig. 10a). Such a metasomatized mantle was subsequently overprinted by metasomatism of low-F melts that derived from the asthenosphere/LVZ (Fig. 10a). The closure of the Paleo-Asian ocean was followed by the closure of the Mongolia-Okhotsk Ocean and the formation of Central Asian Orogenic Belt (CAOB) during the Jurassic to the earliest Cretaceous (Fig. 10b & c; Donskaya et al., 2013; Tomurtogoo et al., 2005). The following breakoff of subducted Mongolia-Okhotsk seafloor slab led to the CAOB region and nearby area in an extension background (Fig. 10d) as manifested by Cretaceous extensional basins and metamorphic core complexes (Davis et al., 2002; Graham et al., 2001). Also for this reason, slab breakoff induced asthenosphere upwelling could produce thermal perturbation at the base of the continental lithosphere and heated the earlier formed metasomatized lithospheirc mantle to faciliate the fusible component melting, producing magmas parental to basalts in this study (Fig. 10d). This model explains the widespread early Cretaceous magmatism that concentrated along the northern margin of the WNCC.

6. Conclusion

The widespread 107.3-133.1 Ma basaltic magmatism in the WNCC originated from partial melting of the metasomatized lithospheric mantle. The mantle source of these basalts contains amphibole/phlogopite, which were formed through metasomatism by low-F melts from asthenosphere mantle and silicic melts derived from the subducted terrigenous sediments. The occurrence of magmatism in WNCC was most probably related to the seafloor slab breakoff following the closure of the Mongolia-Okhotsk ocean, in which scenario upwelling asthenosphere produced thermal perturbation at the base of the lithosphere and heated the lithospheric mantle base, resulting in the melting of the early metasomatized lithospheric mantle materials.

Acknowledgments

We are grateful to Meng Duan, Xiaohong Wang and Hongmei Gong for their assistance with bulk rock major elements analysis, trace elements analysis and Sr-Nd-Hf isotopes compositions analysis, respectively. P.Y. thank Shuo Chen and Huahua Cao for their helpful advice on the manuscript. And we also thank two anonymous reviewers and the editor Xianhua Li for their constructive reviews. This work was supported by the NSFC-Shandong Joint Fund for Marine Science Research Centers (U1606401), the National Natural Science Foundation of China (NSFC Grants 41776067, 41630968, 91014003).

Reference

Abbott, D., Drury, R., Mooney, W., 1997. Continents as lithological icebergs: The importance of buoyant lithospheric roots. Earth and Planetary Science Letters 149, 15-27.

Chen, S., Wang, X.H., Niu, Y.L., Sun, P., Duan, M., Xiao, Y.Y., Guo, P.Y., Gong, H.M., Wang, G.D., Xue, Q.Q., 2017. Simple and cost-effective methods for precise analysis of trace element abundances in geological materials with ICP-MS. Science Bulletin 62, 277-289.

Chen, L., Cheng, C., Wei, Z.G., 2009. Seismic evidence for significant lateral variations in lithospheric thickness beneath the central and western North China Craton. Earth and Planetary Science Letters 286, 171-183.

Cheng, T., Nebel, O., Sossi, P.A., Wu, J., Siebel, W., Chen, F.K., Nebel-Jacobsen, Y.J., 2018. On the Sr-Nd-Pb-Hf isotope code of enriched, Dupal-type sub-continental lithospheric mantle underneath south-western China. Chemical Geology 489, 46-60.

Dai, L.Q., Zheng, Y.F., Zhao, Z.F., 2016. Termination time of peak decratonization in North China: Geochemical evidence from mafic igneous rocks. Lithos 240-243, 327-336.

Davis, G., J. Darby, B., Zheng, Y.D., L. Spell, T., 2002. Geometric and temporal evolution of an extensional detachment fault, Hohhot metamorphic core complex, Inner Mongolia, China. Geology 30, 1003-1006.

Deino, A., Potts, R., 1990. Single-crystal $^{40}Ar/^{39}Ar$ dating of the Olorgesailie Formation, Southern Kenya Rift. Journal of Geophysical Research Solid Earth 95, 8453-8470.

Donskaya, T.V., Gladkochub, D.P., Mazukabzov, A.M., Ivanov, A.V., 2013. Late Paleozoic – Mesozoic subduction-related magmatism at the southern margin of the Siberian continent and the 150 million-year history of the Mongol-Okhotsk Ocean. Journal of Asian Earth Sciences 62, 79-97.

Förster, M.W., Prelević, D., Buhre, S., Mertz-Kraus, R., Foley, S.F., 2019. An experimental study of the role of partial melts of sediments versus mantle melts in the sources of potassic magmatism. Journal of Asian Earth Sciences 177, 76-88.

Gao, S., Luo, T.C., Zhang, B.R., Zhang, H.F., Han, Y.W., Zhao, Z.D., Hu, Y.K., 1998. Chemical composition of the continental crust as revealed by studies in East China. Geochimica et Cosmochimica Acta 62, 1959-1975.

Gao, S., Rudnick, R.L., Xu, W.L., Yuan, H.L., Liu, Y.S., Walker, R.J., Puchtel, I.S., Liu, X.M., Huang,

H., Wang, X.R., Yang, J., 2008. Recycling deep cratonic lithosphere and generation of intraplate magmatism in the North China Craton. Earth and Planetary Science Letters 270, 41-53.

Gao, S., Rudnick, R.L., Yuan, H.L., Liu, X.M., Liu, Y.S., Xu, W.L., Ling, W.L., Ayers, J., Wang, X.C., Wang, Q.H., 2004. Recycling lower continental crust in the North China craton. Nature 432, 892-897.

Graham, S.A., Hendrix, M.S., Johnson, C.L., Badamgarav, D., Badarch, G., Amory, J., Porter, M., Barsbold, R., Webb, L., Hacker, B.R., 2001. Sedimentary record and tectonic implications of Mesozoic rifting in southeast Mongolia. Geological Society of America Bulletin 113, 1560-1579.

Guo, F., Fan, W.M., Wang, Y.J., Lin, G., 2003. Geochemistry of late mesozoic mafic magmatism in west Shandong Province, eastern China: Characterizing the lost lithospheric mantle beneath the North China Block. Geochemical Journal 37, 63-77.

Guo, J.T., Guo, F., Yan Wang, C., Li, C.W., 2013. Crustal recycling processes in generating the early Cretaceous Fangcheng basalts, North China Craton: New constraints from mineral chemistry, oxygen isotopes of olivine and whole-rock geochemistry. Lithos 170-171, 1-16.

Guo, P.Y., Niu, Y.L., Sun, P., Wang, X.H., Gong, H.M., Duan, M., Zhang, Y., Kong, J.J., Tian, L.Y., Wu, S.G., 2018. The Early Cretaceous bimodal volcanic suite from the Yinshan Block, western North China Craton: Origin, process and geological significance. Journal of Asian Earth Sciences 160, 348-364.

Guo, P.Y., Niu, Y.L., Ye, L., Liu, J.J., Sun, P., Cui, H.X., Zhang, Y., Gao, J.P., Su, L., Zhao, J.X., Feng, Y.X., 2014. Lithosphere thinning beneath west North China Craton: Evidence from geochemical and Sr–Nd–Hf isotope compositions of Jining basalts. Lithos 202-203, 37-54.

Hawkesworth, C. J., Gallagher, K., Hergt, J. M., & McDermott, F. (1993). Mantle and slab contributions in arc magmas. Annual Review of Earth and Planetary Sciences, 21(1), 175–204.

He, Y.K., Wu, T.R., Jin, X., 2013. $^{40}Ar/^{39}Ar$ Laser Probe Dating of Siziwangqi Shoshonite and Its Geological Significance. Geology and Exploration 49, 1114-1122 (in Chinese with English abstract).

Hui, J., Cheng, H.Y., Zhang, J., Zhang, K.J., Qu, J.F., Zhang, B.H., 2020. Early Cretaceous continent basalts in the Alxa Block, NW China: geochronology, geochemistry, and tectonic implications. International Geology Review, 1-18.

Jordan, T., 1988. Structure and Formation of the Continental Tectosphere. Journal of Petrology Special

Volume, 11-37.

Kong, J.J., Niu, Y.L., Sun, P., Xiao, Y.Y., Guo, P.Y., Hong, D., Zhang, Y., Shao, F.L., Wang, X.H., Duan, M., 2019. The origin and geodynamic significance of the Mesozoic dykes in eastern continental China. Lithos 332-333, 328-339.

Le Bas, M., Maitre, L., L. Streckeisen, A., B. A, Z., 1986. A Chemical Classification of Volcanic Rocks Based on the Total Alkali-Silica Diagram. Journal of Petrology 27, 745-750.

Le Maitre, R.W., Bateman, P., Dudek, A., Keller, J., Lameyre, J., Le Bas, M.J., Sabine, P.A., Schmid, R., Sorensen, H., Streckeisen, A., Wooley, A.R., Zanettin, B., 1989. A Classification of igneous rocks and glossary of terms. Oxford: Blackwell.

Li, J.Y., 2006. Permian geodynamic setting of Northeast China and adjacent regions: closure of the Paleo-Asian Ocean and subduction of the Paleo-Pacific Plate. Journal of Asian Earth Sciences 26, 207-224.

Li, Y., Xu, W.L., Tang, J., Pei, F.P., Wang, F., Sun, C.Y., 2018. Geochronology and geochemistry of Mesozoic intrusive rocks in the Xing'an Massif of NE China: Implications for the evolution and spatial extent of the Mongol–Okhotsk tectonic regime. Lithos 304-307, 57-73.

Ling, W.L., Duan, R.C., Xie, X.J., Zhang, Y.Q., Zhang, J.B., Cheng, J.P., Liu, X.M., Yang, H.M., 2009. Contrasting geochemistry of the Cretaceous volcanic suites in Shandong province and its implications for the Mesozoic lower crust delamination in the eastern North China craton. Lithos 113, 640-658.

Liu, D.Y., Nutman, A.P., Compston, W., Wu, J.S., Shen, Q.H., 1992. Remnants of ≥3800 Ma crust in the Chinese part of the Sino-Korean craton. Geology 20, 339-342.

Liu, Y.S., Gao, S., Kelemen, P.B., Xu, W.L., 2008. Recycled crust controls contrasting source compositions of Mesozoic and Cenozoic basalts in the North China Craton. Geochimica et Cosmochimica Acta 72, 2349-2376.

Liu, Y.S., Gao, S., Yuan, H.L., Zhou, L., Liu, X.M., Wang, X.C., Hu, Z.C., Wang, L.S., 2004. U–Pb zircon ages and Nd, Sr, and Pb isotopes of lower crustal xenoliths from North China Craton: insights on evolution of lower continental crust. Chemical Geology 211, 87-109.

Ma, L., Jiang, S.-Y., Hofmann, A.W., Dai, B.-Z., Hou, M.-L., Zhao, K.-D., Chen, L.-H., Li, J.-W., Jiang, Y.-H., 2014. Lithospheric and asthenospheric sources of lamprophyres in the Jiaodong Peninsula: A consequence of rapid lithospheric thinning beneath the North China Craton? Geochimica et Cosmochimica Acta 124, 250-271.

Meng, F.X., Gao, S., Niu, Y.L., Liu, Y.S., Wang, X.R., 2015. Mesozoic–Cenozoic mantle evolution beneath the North China Craton: A new perspective from Hf–Nd isotopes of basalts. Gondwana Research 27, 1574-1585.

Niu, Y.L., O'Hara, M.J., 2003. Origin of ocean island basalts: A new perspective from petrology, geochemistry, and mineral physics considerations. Journal of Geophysical Research: Solid Earth 108.

Niu, Y.L., 2008. The Origin of Alkaline Lavas. Science 320, 883-884.

Niu, Y.L., 2005. Generation and Evolution of Basaltic Magamas: Some Basic Concepts and a New View on the Origin of Mesozoix- Cenozoic Basaltic Volcanism in Eastern China. Geological Journal of China Universities 11, 9-46.

Niu, Y.L., Wilson, M., Humphreys, E.R., O'Hara, M.J., 2012. A trace element perspective on the source of ocean island basalts (OIB) and fate of subducted ocean crust (SOC) and mantle lithosphere (SML). Episodes. 35, 310-327.

Niu, Y.L., 2014. Geological understanding of plate tectonics: Basic concepts, illustrations, examples and new perspectives. Global Tectonics and Metallogeny 10, 23-46.

Ouyang, H., Mao, J., Zhou, Z., Su, H., 2015. Late Mesozoic metallogeny and intracontinental magmatism, southern Great Xing'an Range, northeastern China. Gondwana Research 27, 1153-1172.

Pilet, S., Baker, M.B., Stolper, E.M., 2008. Metasomatized Lithosphere and the Origin of Alkaline Lavas. Science 320, 916-919.

Pilet, S., Baker, M.B., Müntener, O., Stolper, E.M., 2011. Monte Carlo Simulations of Metasomatic Enrichment in the Lithosphere and Implications for the Source of Alkaline Basalts. Journal of Petrology 52, 1415-1442.

Plank, T., Langmuir, C.H., 1998. The chemical composition of subducting sediment and its consequences for the crust and mantle. Chemical Geology 145, 325-394.

Renne, P.R., Cassata, W.S., Morgan, L.E., 2009. The isotopic composition of atmospheric argon and Ar/Ar geochronology: Time for a change? Quaternary Geochronology 4, 288-298.

Ringwood A E., 1975. Composition and Petrology of the Earth's Mantle. New York : McCraw-Hill , 618.

Sekine, T., Wyllie, P.J., 1983. Experimental Simulation of Mantle Hybridization in Subduction Zones. The Journal of Geology 91, 511-528.

Shi, Y.N., Niu, F.L., Li, Z.H., Huangfu, P., 2020. Craton destruction links to the interaction between

subduction and mid-lithospheric discontinuity: Implications for the eastern North China Craton. Gondwana Research 83, 49-62.

Soder, C., Altherr, R., Romer, R.L., 2016. Mantle Metasomatism at the Edge of a Retreating Subduction Zone: Late Neogene Lamprophyres from the Island of Kos, Greece. Journal of Petrology 57, 1705-1728.

Stracke, A., Bizimis, M., Salters, V.J.M., 2003. Recycling oceanic crust: Quantitative constraints. Geochemistry, Geophysics, Geosystems 4, 1-33.

Stracke, A., Hofmann, A., Hart, S., 2005. FOZO, HIMU, and the rest of the mantle zoo. Geochemistry, Geophysics, Geosystems 6(5), 1-20.

Sun, P., Niu, Y.L., Guo, P.Y., Chen, S., Duan, M., Gong, H.M., Wang, X.H., Xiao, Y.Y., 2019. Multiple mantle metasomatism beneath the Leizhou Peninsula, South China: evidence from elemental and Sr-Nd-Pb-Hf isotope geochemistry of the late Cenozoic volcanic rocks. International Geology Review 61, 1768-1785.

Sun, S.S., McDonough, W.F., 1989. Chemical and isotopic systematics of oceanic basalts: implications for mantle composition and processes. Geological Society, London, Special Publications 42, 313-345.

Tiepolo, M., Bottazzi, P., Foley, S., Oberti, R., Vannucci, R., Zanetti, A., 2001. Fractionation of Nb and Ta from Zr and Hf at mantle depths: the role of titanian pargasite and kaersutite. Journal of Petrology 42, 221-232.

Tomurtogoo, O., Windley, B.F., Kroner, A., Badarch, G., Liu, D.Y., 2005. Zircon age and occurrence of the Adaatsag ophiolite and Muron shear zone, central Mongolia: constraints on the evolution of the Mongol-Okhotsk ocean, suture and orogen. Journal of the Geological Society 162, 125-134.

Vasconcelos, P.N., Onoe, A.T., Kawashita, K., Soares, A.J., Teixeira, W., 2002. $^{40}Ar/^{39}Ar$ geochronology at the Instituto de Geociencias, USP: instrumentation, analytical procedures, and calibration. Anais Da Academia Brasileira De Ciencias 74, 297-342.

Vervoort, J.D., Blichert-Toft, J., 1999. Evolution of the depleted mantle: Hf isotope evidence from juvenile rocks through time. Geochimica et Cosmochimica Acta 63, 533-556.

Wang, C.Y., Liu, Y.S., Foley, S.F., Zong, K.Q., Hu, Z.C., 2019. Lithospheric transformation of the northern North China Craton by changing subduction style of the Paleo-Asian oceanic plate: Constraints from peridotite and pyroxenite xenoliths in the Yangyuan basalts. Lithos 328-329, 58-68.

Wilde, S.A., 2015. Final amalgamation of the Central Asian Orogenic Belt in NE China: Paleo-Asian Ocean closure versus Paleo-Pacific plate subduction — A review of the evidence. Tectonophysics 662, 345-362.

Workman, R.K., Hart, S.R., 2005. Major and trace element composition of the depleted MORB mantle (DMM). Earth and Planetary Science Letters 231, 53-72.

Wu, F.Y., Walker, R.J., Yang, Y.H., Yuan, H.L., Yang, J.H., 2006. The chemical-temporal evolution of lithospheric mantle underlying the North China Craton. Geochimica et Cosmochimica Acta 70, 5013-5034.

Wu, F.Y., Xu, Y.G., Gao, S., Zheng, J.P., 2008. Lithospheric thinning and destruction of the North China Craton. Acta Petrologica Sinica 24, 1145-1174 (in Chinese with English abstract).

Wyllie, P.J., Sekine, T., 1982. The formation of mantle phlogopite in subduction zone hybridization. Contributions to Mineralogy and Petrology 79, 375-380.

Xiao, W.J., Windley, B., Hao, J.J., Zhai, M.G., 2003. Accretion leading to collision and the Permian Solonker suture, Inner Mongolia, China: Termination of the Central Asian Orogenic Belt. Tectonics 22.

Xiong, X.L., Adam, J., Green, T.H., 2005. Rutile stability and rutile/melt HFSE partitioning during partial melting of hydrous basalt: Implications for TTG genesis. Chemical Geology 218, 339-359.

Yang, D.B., Xu, W.L., Pei, F.P., Yang, C.H., Wang, Q.H., 2012. Spatial extent of the influence of the deeply subducted South China Block on the southeastern North China Block: Constraints from Sr–Nd–Pb isotopes in Mesozoic mafic igneous rocks. Lithos 136-139, 246-260.

Yang, Y.H., Zhang, H.F., Xie, L.W., Liu, Y., Qi, C.S., Tu, X.L., 2006. Petrogenesis of typical Mesozoic and Cenozoic volcanic rocks from the North China Craton: new evidence from Hf isotopic studies. Acta Petrologica Sinica 22, 1665-1671 (in Chinese with English abstract).

Zhang, H.F., Sun, M., Zhou, X.H., Fan, W.M., Zhai, M.G., Yin, J.F., 2002. Mesozoic lithosphere destruction beneath the North China Craton: evidence from major-, trace-element and Sr–Nd–Pb isotope studies of Fangcheng basalts. Contributions to Mineralogy and Petrology 144, 241-254.

Zhang, H.F., Sun, M., Zhou, X.H., Zhou, M.F., Fan, W.M., Zheng, J.P., 2003. Secular evolution of the lithosphere beneath the eastern North China Craton: evidence from Mesozoic basalts and high-Mg andesites. Geochimica et Cosmochimica Acta 67, 4373-4387.

Zhang, H.F., Sun, Y.L., Tang, Y.J., Xiao, Y., Zhang, W.H., Zhao, X.M., Santosh, M., Menzies, M.A., 2012. Melt-peridotite interaction in the Pre-Cambrian mantle beneath the western North China Craton: Petrology, geochemistry and Sr, Nd and Re isotopes. Lithos 149, 100-114.

Zhang, P.F., 2013. Geochemical characteristics and Pettrogenesis of the Volcanic Rocks from the Middle of the Yinshan Block. The University of Chinese Academy of Sciences.

Zhang, S.H., Zhao, Y., Song, B., Hu, J.M., Liu, S.W., Yang, Y.H., Chen, F.K., Liu, X.M., Liu, J., 2009. Contrasting Late Carboniferous and Late Permian–Middle Triassic intrusive suites from the northern margin of the North China craton: Geochronology, petrogenesis, and tectonic implications. GSA Bulletin 121, 181-200.

Zhang, S.T., Wu, T.R., Xu, X., Byamba, J., Amarjargal, A., Wang, S.Q., Li, Z.Q., 2005. The Siginificance of Discovery of Early Cretaceous Shoshonite in Central Inner Monglia. Acta Scientiarum Naturalium Universitatis Pekinesis 41, 212-218 (in Chinese with English abstract).

Zhao, G.C., Sun, M., Wilde, S.A., Li, S.Z., 2005. Late Archean to Paleoproterozoic evolution of the North China Craton: key issues revisited. Precambrian Research 136, 177-202.

Zhao, G.C., Wilde, S.A., Cawood, P.A., Sun, M., Cruden, A.R., Easton, R.M., 2001. Archean blocks and their boundaries in the North China Craton; lithological, geochemical, structural and P-T path constraints and tectonic evolution. Precambrian Research 107, 45-73.

Zhao, Y., Zheng, J.P., Xiong, Q., Zhang, H., 2018. Destruction of the North China Craton triggered by the Triassic Yangtze continental subduction/collision: A review. Journal of Asian Earth Sciences 164, 72-82.

Zhong, F.P., Zhong, J.H., Abdurahman, A., Wang, Y., You, W.F., Yang, W.L., 2015. Timing and scale of the destruction of the North China craton: Revelation from the early cretaceous volcanic rocks in Suhongtu Depression of Inggen-Ejin Banner Basin. Geology in China 42, 435-456 (in Chinese with English abstract).

Zhong, F.P., Zhong, J.H., Wang, Y., Tian, W.F., 2014. Geochemistry Charaacteristics and Origin of Early Cretaceous Volcanic Rocks in Suhongtu Depression, Inner Mongolia, China. Acta Mineralogica sinica 34, 107-116 (in Chinese with English abstract).

Zhu, R.X., Chen, L., Wu, F.Y., Liu, J.L., 2011. Timing, scale and mechanism of the destruction of the North China Craton. Science China Earth Sciences 54, 789-797.

631 Zhu, R.X., Pan, Y.X., He, H.Y., Qin, H.F., Ren, S.M., 2008. Palaeomagnetism and $^{40}Ar/^{39}Ar$ age from a
632 Cretaceous volcanic sequence, Inner Mongolia, China: Implications for the field variation during the
633 Cretaceous normal superchron. Physics of the Earth and Planetary Interiors 169, 59-75.
634 Zou, H.P., Zhang, K., Li, G., 2008. Cretacaous tectono-thermal event in the Ordos Block: an Ar-Ar
635 Chronological evidence from basalt at Hangjin banner, inner Monggolia, north China craton.
636 Geotectonica et Metallogenia 32, 360-364 (in Chinese with Enflish abstract).
637

638 **Figure Captions**

639 **Fig. 1** (a) Sketch map of major tectonic divisions of the North China Craton (modified from Shi et al
640 (2020) and Zhao et al(2001)). Also shown are the early Cretaceous volcanism in the WNCC. (b) The
641 distribution and sample locations of the Wulate Zhongqi basalts.

642 **Fig. 2** Representative field photographs and petrography. (a) Volcanic rock outcrop in Wulate Zhongqi.
643 (b) Volcanic rock outcrop in Heishitougou. (c)-(f) Petrography of the basalts and andesitic basalts from
644 Wulate Zhongqi and Heishitougou. Pl- plagioclase; Mag- magnetite; Px- pyroxene; Ol- olivine.

645 **Fig. 3** Ar-Ar age spectra and $^{39}Ar/^{40}Ar$ vs. $^{36}Ar/^{40}Ar$ correlation of the whole rock sample ZQ14-47 from
646 Wulate Zhongqi.

647 **Fig. 4** MgO-variation diagrams showing major element oxides, CaO/Al_2O_3, Cr and Ni for basalts from
648 Wulate Zhongqi and Heishitougou. Arrows decreasing MgO approximate first-order trends dominated
649 by fractional crystallization. The arrows in the right represent the effect of fractional crystallization of
650 different minerals. Plag- plagioclase; Cpx- clinopyroxene; Ol- olivine.

651 **Fig. 5** Chondrite-normalized rare earth element and primitive mantle normalized incompatible element
652 patterns for basalts from Wulate Zhongqi and Heishitougou. Chondrite and primitive mantle values are
653 from Sun and McDonough (1989). For comparison, plotted also are average composition of present-day
654 oceanic island basalts (OIB; Sun and McDonough, 1989), global subducted sediment (GLOSS, Plank
655 and Langmuir, 1998), average crust of NCC (Gao et al., 1998) and the range of >110Ma Basalts from the
656 ENCC (Dai et al., 2016; Liu et al., 2008).

657 **Fig. 6** Sr, Nd and Hf isotope compositions of basalts from Wulate Zhongqi and Heishitougou. Plotted
658 also are the literature data of >110Ma Mesozoic basalts from the ENCC (Dai et al., 2016; Gao et al.,
659 2008; Guo et al., 2003; Guo et al., 2013; Ling et al., 2009; Meng et al., 2015; Yang et al., 2012; Yang et

al., 2006; Zhang et al., 2002, 2003), Early Createcous basalts from WNCC (Guo et al., 2014, 2018) and Paleozoic kimberlite and mantle xenoliths (Wu et al., 2006 and references therein). Reference Terrestrial Array (ε_{Hf}=1.36ε_{Nd}+2.95) is after Vervoort and Blichert-Toft (1999). Also shown are the present-day compositions of oceanic island basalts (OIB) and mid-ocean ridge basalts (MORB) (Stracke et al., 2003; Stracke et al., 2005). R value (correlation coefficient) of WNCC basalts was calculated excluding ZQ14-29.

Fig. 7 $\varepsilon_{Hf}(t)$ vs. MgO/SiO_2 and Nb/La diagrams to show crustal materials contamination play negligible role in the most WNCC basalts, except for ZQ14-09, ZQ14-26, ZQ14-52 and ZQ19-08.

Fig. 8 (a) and (c) are P/Nd and Nb/La vs. $\varepsilon_{Nd(t)}$ diagrams; (b) and (d) are P/Nd and Nb/La vs. $\varepsilon_{Hf(t)}$ diagrams; (e) Nb/La vs. Sm/Nd diagrams and (f) Nb/Th vs. Lu/Hf diagrams to show both the terrigenous sediments and low-F melts contribution in the formation of the enriched mantle source of the WNCC basalts. We select N-MORB (Sun and McDonough, 1989; Workman and Hart, 2005), represented by yellow star, as the magma from partial melting of depleted mantle source and red star represents global subducted sediment (GLOSS, Plank and Langmuir, 1998). The Double-headed arrows represent the variation trends of the incompatible element ratios caused by the contribution of different metasomatism agents.

Fig. 9 Trace element modelling of the multiple metasomatism melts in the mantle source region of the basalts in Wulate Zhongqi and Heishitougou. We approximate basalts from Siziwangqi as the result of partial melts derived from low-F melts metasomatized mantle (Guo et al., 2014) and choose global subducted sediments (GLOSS, Plank and Langmuir, 1998) as the end-members of subducted terrigenous sediments. The percentage in the figure (20%, 40%, 60%) means proportion of sediment.

Fig. 10 Graphical description of the petrogenesis of the early Cretaceous basalts in the WNCC. (a) The Paleo-Asian ocean slab subducted southward underneath the North China Craton in the late Paleozoic

and contributed terrigenous sediments into the mantle; and the silica-melts derived from the subduced terrigenous sediments and low-F melts from asthenosphere metasomatized the overlying lithospheric mantle, forming metasomatic veins at the base of the lithosphere; (b) The Paleo-Asian ocean was closed in the early Mesozoic, leading to the orogenesis of the Central Asian Orogenic Belt (CAOB); (c) the Mongolia-Okhotsk ocean closed in the Triassic to Middle Jurassic; (d) Breakoff of subducted Mongol-Okhotsk oceanic slabs resulted in an upwelling of the asthenosphere, and such upwelling asthenosphere produced thermal perturbation at the base of the lithosphere and heated the lithospheric mantle. The fusiable metasomatized components were, thus, melted and produced the primary magmas parental to the baslats in this study. SLS in the figure indicated Solonker suture zone.

Fig. S1 (a) The K_2O+Na_2O vs. SiO_2 diagram (Le Bas et al., 1986) and (b) K_2O vs. SiO_2 diagram (Le Maitre et al., 1989) for basalts from Wulate Zhongqi and Heishitougou, for which, all the data plotted have been normalized to 100% on a volatile-free basis.

Fig. S2 Variation of selected trace element versus Zr for the Wulate Zhongqi and Heishitougou basalts. R^2 is the square of correlation coefficients of Wulate Zhongqi Basalts.

Figure

Fig. 1

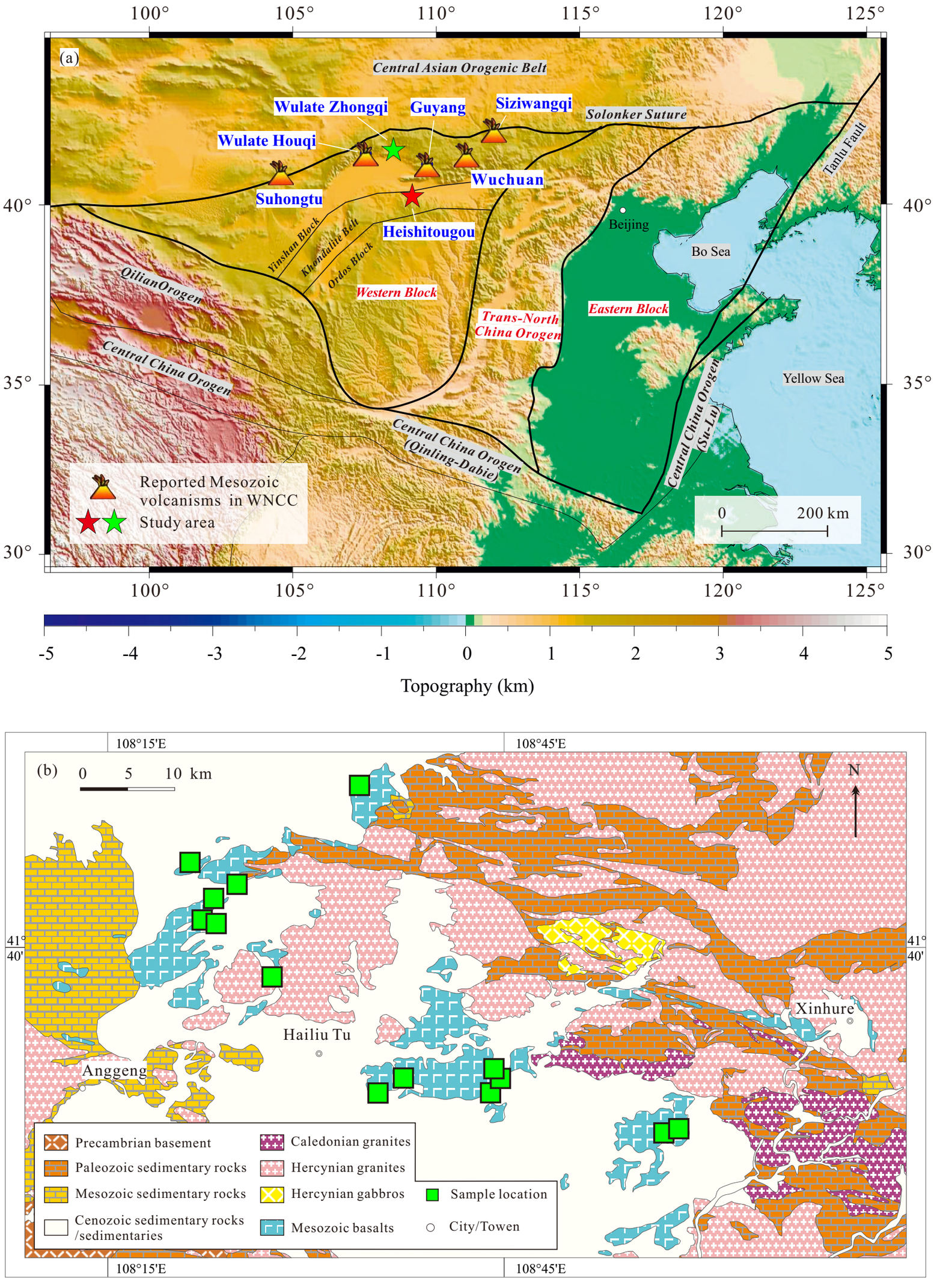
(a)
Central Asian Orogenic Belt
Wulate Zhongqi
Guyang
Siziwangqi
Solonker Suture
Wulate Houqi
Wuchuan
Suhongtu
Heishitougou
Yinshan Block
Khondalite Belt
Ordos Block
Western Block
Eastern Block
Trans-North China Orogen
QilianOrogen
Central China Orogen
Central China Orogen (Qinling-Dabie)
Central China Orogen (Su-Lu)
Tanlu Fault
Beijing
Bo Sea
Yellow Sea
Reported Mesozoic volcanisms in WNCC
Study area
0
200 km
100°
105°
110°
115°
120°
125°
40°
35°
30°
-5
-4
-3
-2
-1
0
1
2
3
4
5
Topography (km)
(b)
0 5 10 km
N
108°15'E
108°45'E
41°
40'
Hailiu Tu
Anggeng
Xinhure
Precambrian basement
Paleozoic sedimentary rocks
Mesozoic sedimentary rocks
Cenozoic sedimentary rocks /sedimentaries
Caledonian granites
Hercynian granites
Hercynian gabbros
Mesozoic basalts
Sample location
City/Towen

Fig. 2

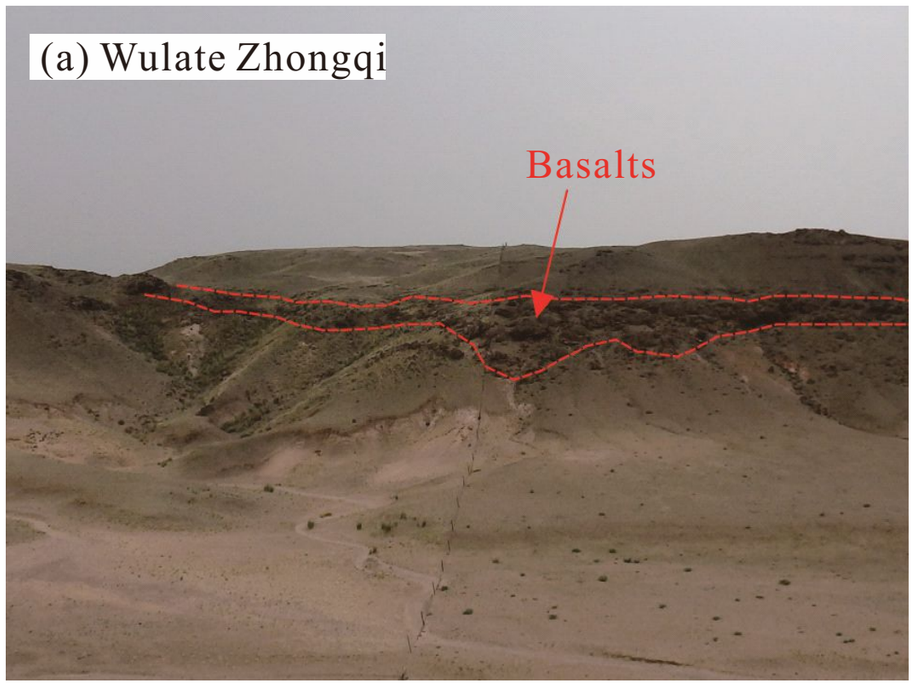
(a) Wulate Zhongqi
Basalts


(b) Heishitougou

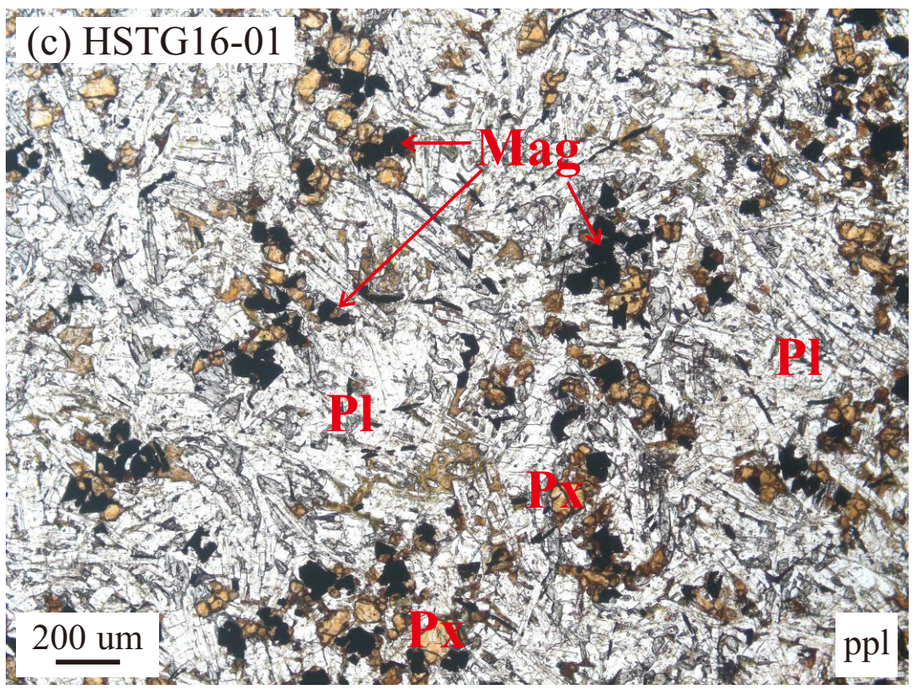
(c) HSTG16-01
Mag
Pl
Pl
Px
Px
200 um
ppl

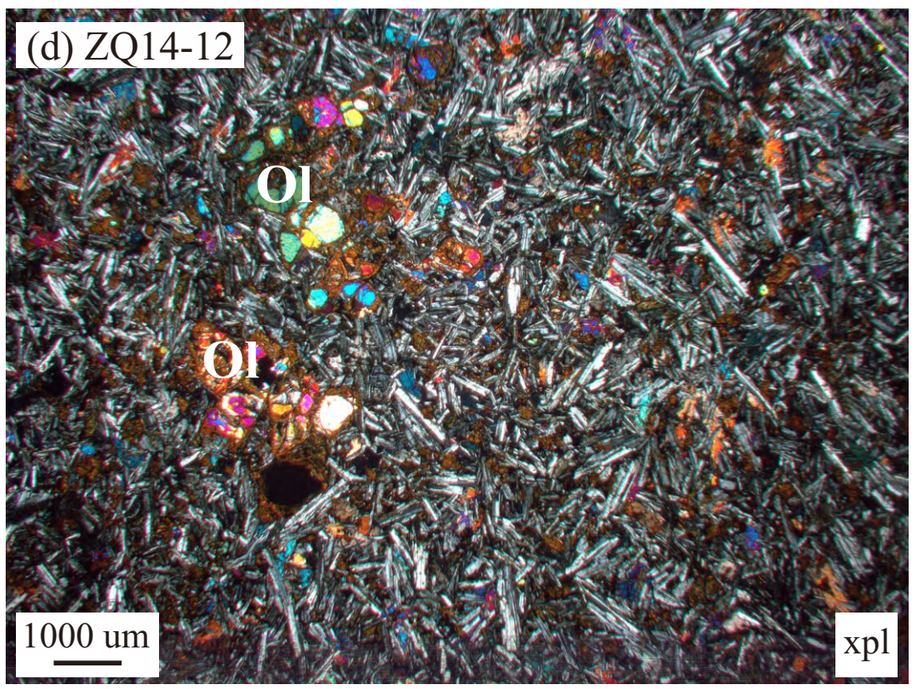
(d) ZQ14-12
Ol
Ol
1000 um
xpl

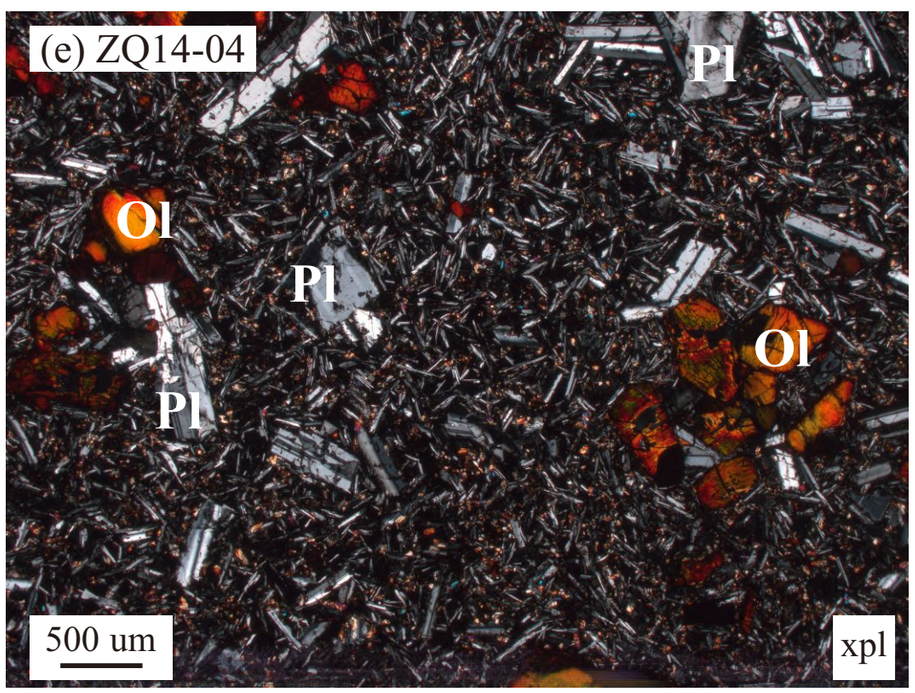
(e) ZQ14-04
Pl
Ol
Pl
Ol
Pl
500 um
xpl

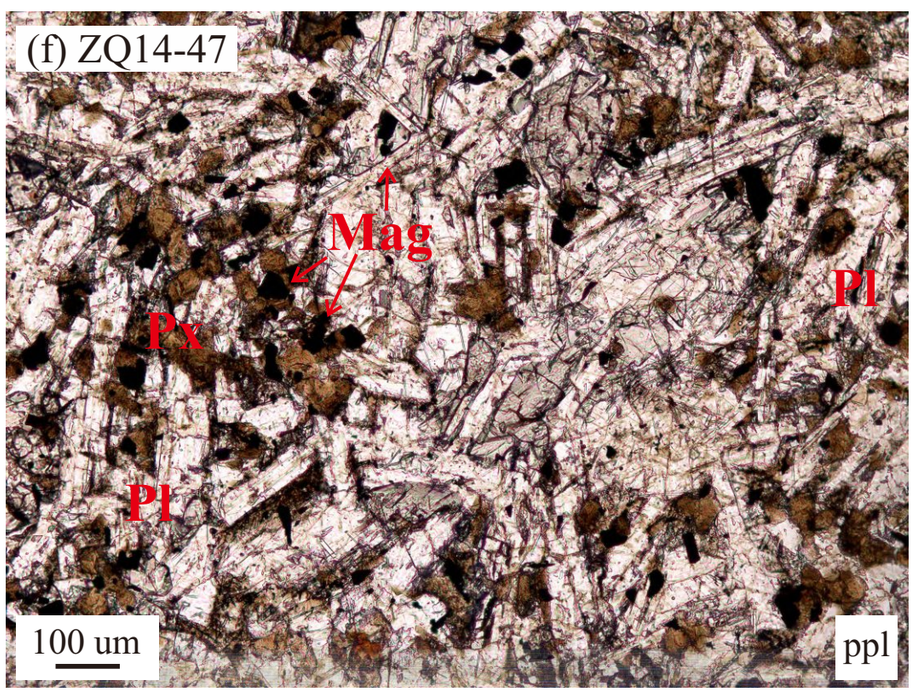
(f) ZQ14-47
Mag
Px
Pl
Pl
100 um
ppl

Fig. 3

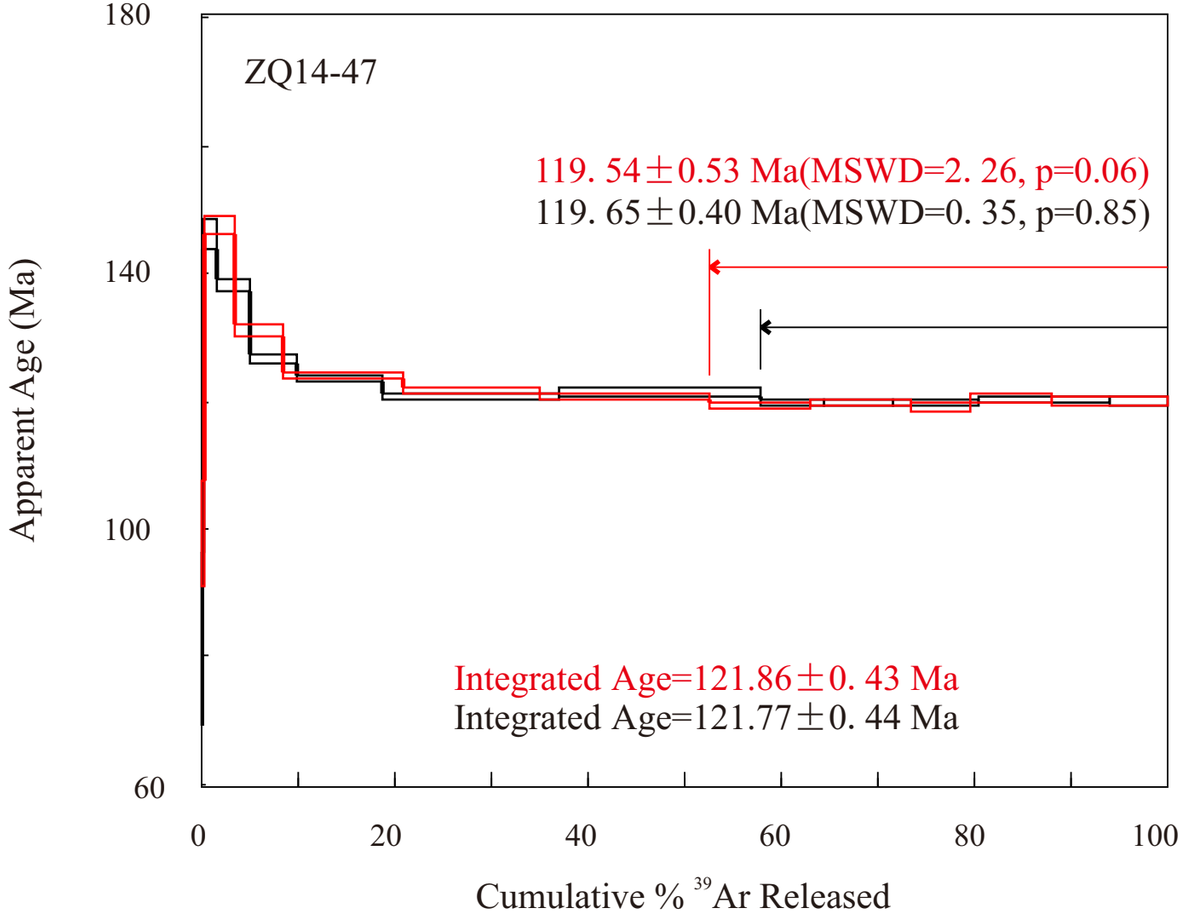
ZQ14-47
119. 54±0.53 Ma(MSWD=2. 26, p=0.06)
119. 65±0.40 Ma(MSWD=0. 35, p=0.85)
Integrated Age=121.86±0. 43 Ma
Integrated Age=121.77±0. 44 Ma
Apparent Age (Ma)
180
140
100
60
0
20
40
60
80
100
Cumulative % 39Ar Released

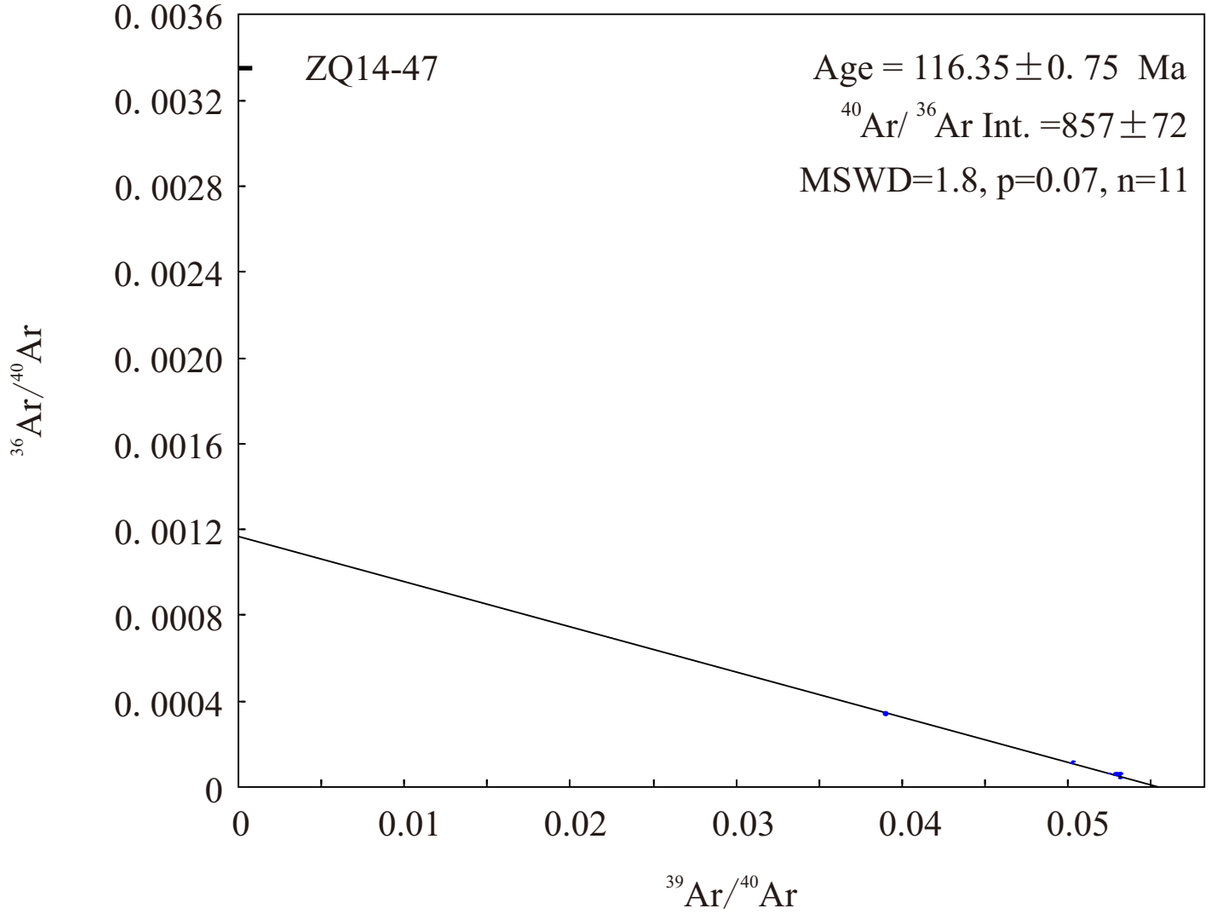
ZQ14-47
Age = 116.35±0. 75 Ma
40Ar/ 36Ar Int. =857±72
MSWD=1.8, p=0.07, n=11
36Ar/40Ar
0. 0036
0. 0032
0. 0028
0. 0024
0. 0020
0. 0016
0. 0012
0. 0008
0. 0004
0
0
0.01
0.02
0.03
0.04
0.05
39Ar/40Ar

Fig. 4

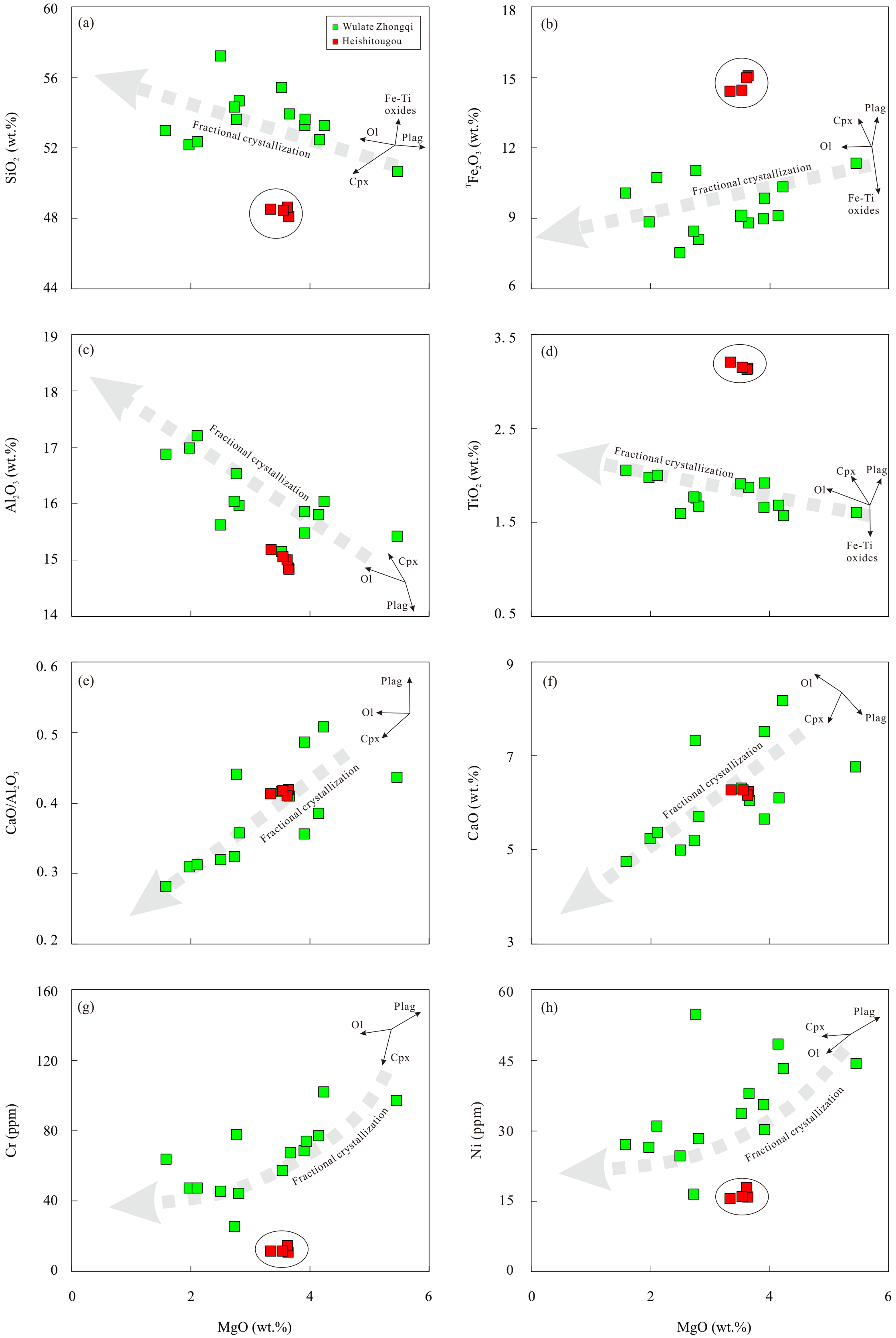
(a)
Wulate Zhongqi
Heishitougou
Fe-Ti oxides
Ol
Plag
Cpx
Fractional crystallization
SiO2 (wt.%)
60
56
52
48
44
(b)
Plag
Cpx
Ol
Fe-Ti oxides
Fractional crystallization
TFe2O3 (wt.%)
18
15
12
9
6
(c)
Fractional crystallization
Cpx
Ol
Plag
Al2O3 (wt.%)
19
18
17
16
15
14
(d)
Fractional crystallization
Cpx
Plag
Ol
Fe-Ti oxides
TiO2 (wt.%)
3. 5
2. 5
1. 5
0. 5
(e)
Plag
Ol
Cpx
Fractional crystallization
CaO/Al2O3
0. 6
0. 5
0. 4
0. 3
0. 2
(f)
Ol
Cpx
Plag
Fractional crystallization
CaO (wt.%)
9
7
5
3
(g)
Plag
Ol
Cpx
Fractional crystallization
Cr (ppm)
160
120
80
40
0
0
2
4
6
MgO (wt.%)
(h)
Plag
Cpx
Ol
Fractional crystallization
Ni (ppm)
60
45
30
15
0
0
2
4
6
MgO (wt.%)

Fig.5

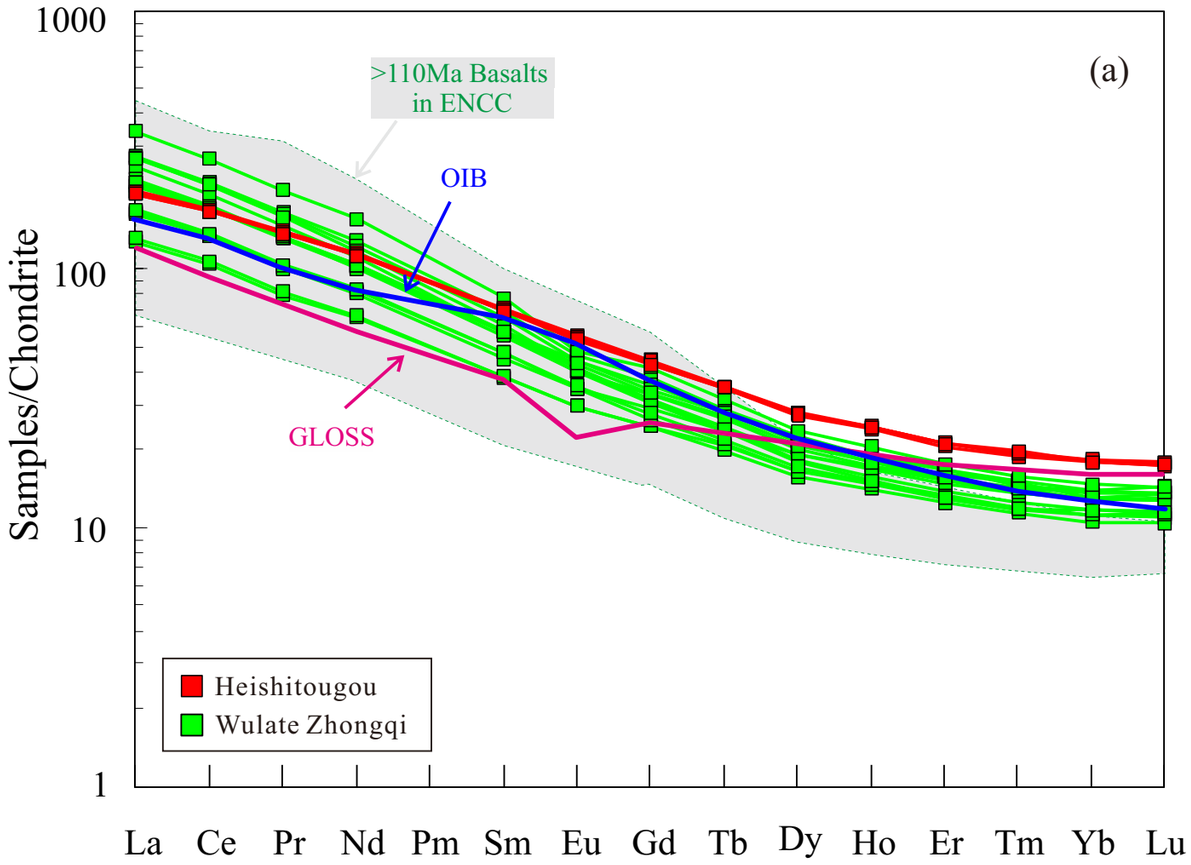
1000
100
10
1
Samples/Chondrite
(a)
>110Ma Basalts
in ENCC
OIB
GLOSS
Heishitougou
Wulate Zhongqi
La Ce Pr Nd Pm Sm Eu Gd Tb Dy Ho Er Tm Yb Lu

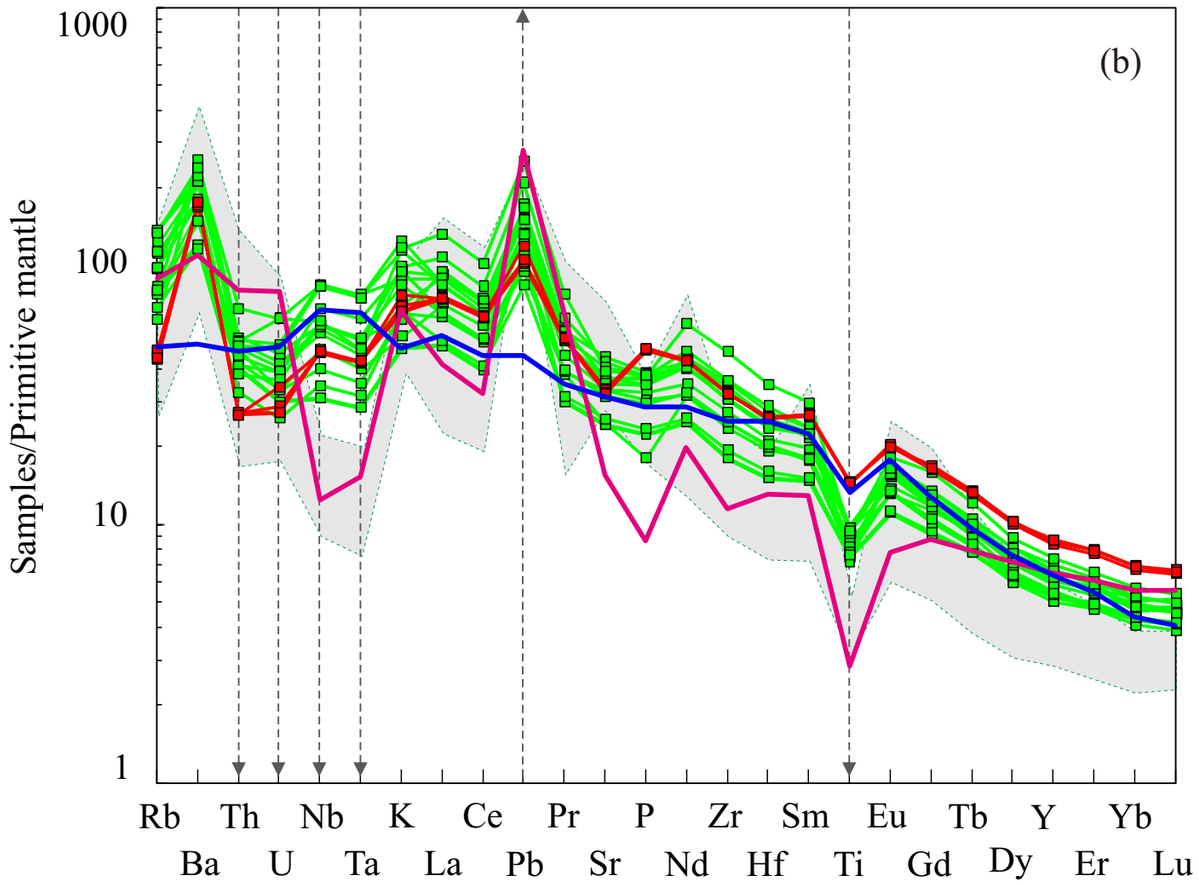
1000
100
10
1
Samples/Primitive mantle
(b)
Rb Ba Th U Nb Ta K La Ce Pb Pr Sr P Nd Zr Hf Sm Ti Eu Gd Tb Dy Y Er Yb Lu

Fig. 6

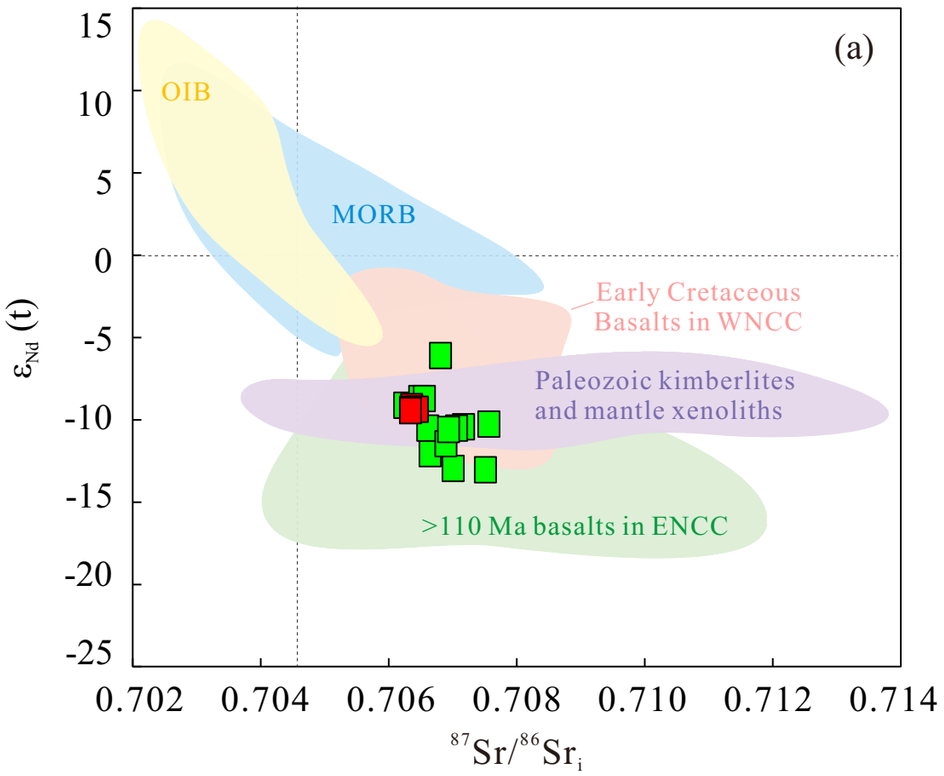
(a)
OIB
MORB
Early Cretaceous
Basalts in WNCC
Paleozoic kimberlites
and mantle xenoliths
>110 Ma basalts in ENCC
15
10
5
0
-5
-10
-15
-20
-25
0.702
0.704
0.706
0.708
0.710
0.712
0.714
εNd (t)
87Sr/86Sri

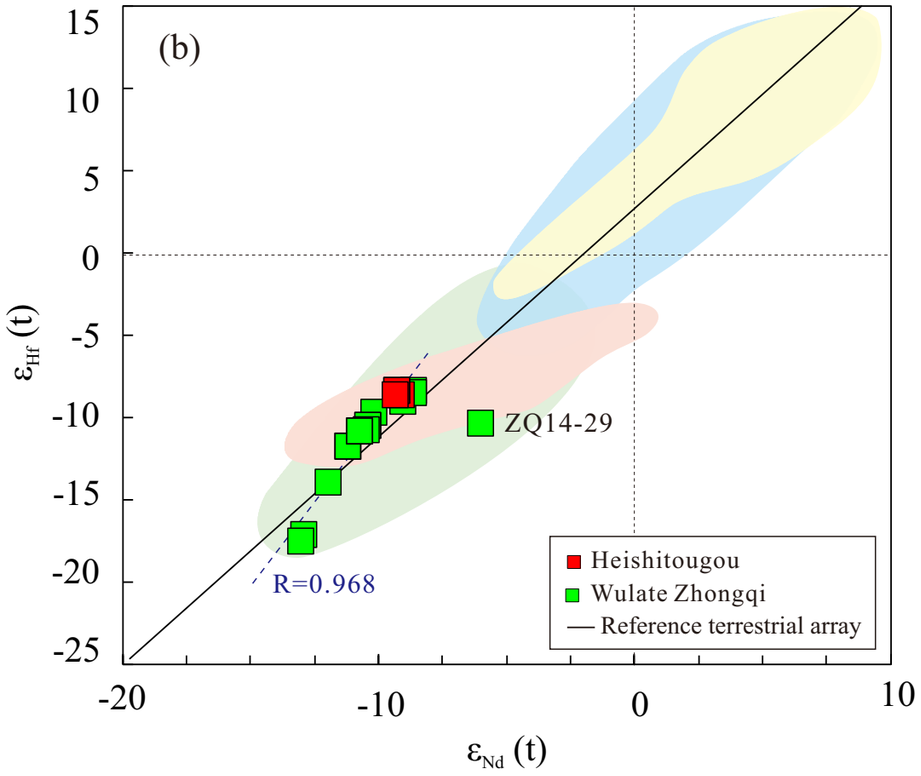
(b)
ZQ14-29
R=0.968
Heishitougou
Wulate Zhongqi
Reference terrestrial array
15
10
5
0
-5
-10
-15
-20
-25
-20
-10
0
10
εHf (t)
εNd (t)

Fig.7

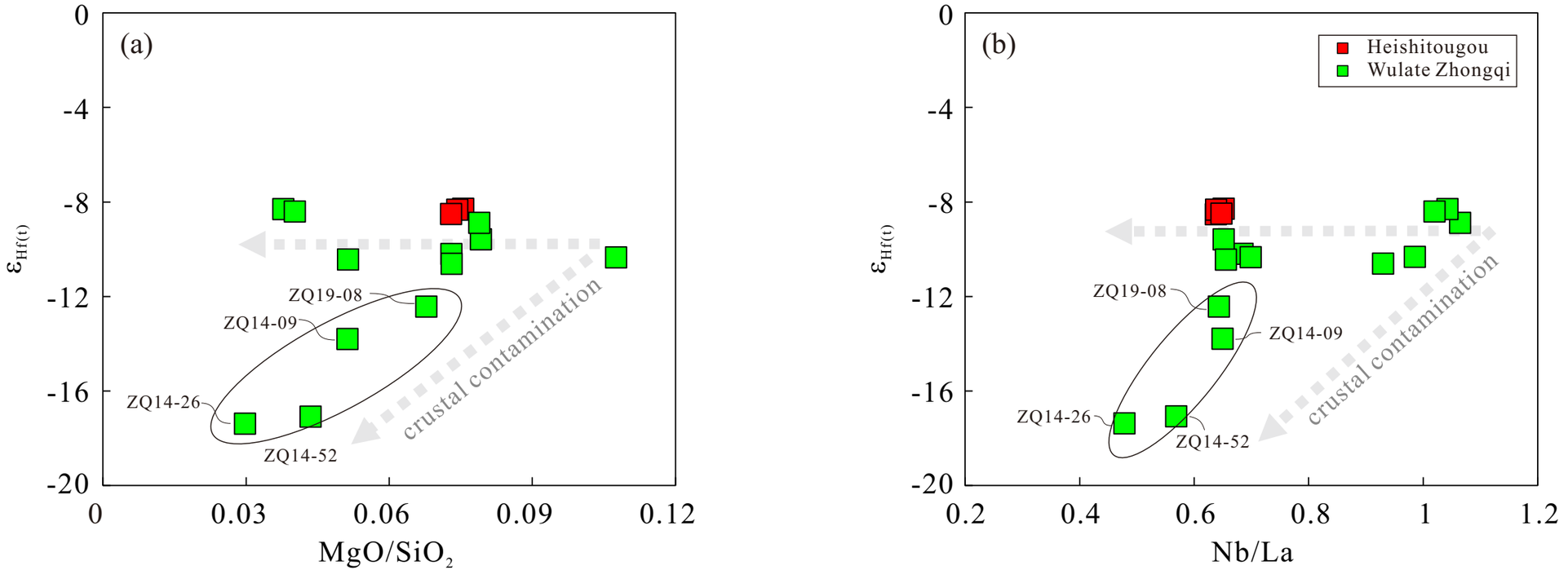
(a)
(b)
Heishitougou
Wulate Zhongqi
ZQ19-08
ZQ14-09
ZQ14-26
ZQ14-52
crustal contamination
$\varepsilon_{Hf(t)}$
MgO/SiO$_2$
Nb/La
0
-4
-8
-12
-16
-20
0.03
0.06
0.09
0.12
0.2
0.4
0.6
0.8
1
1.2

Fig.8

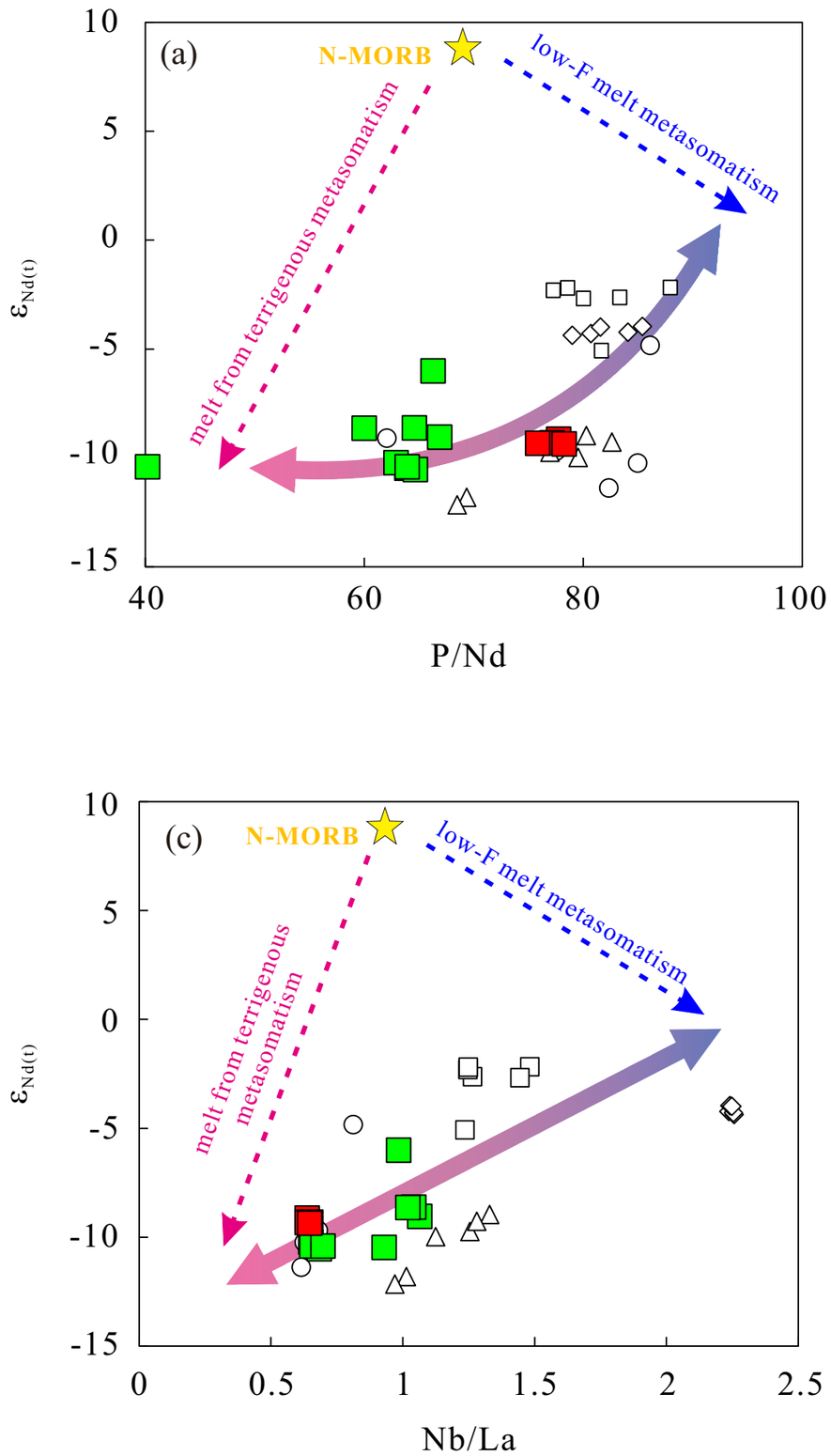
(a)
N-MORB
low-F melt metasomatism
melt from terrigenous metasomatism
$\varepsilon_{Nd(t)}$
P/Nd

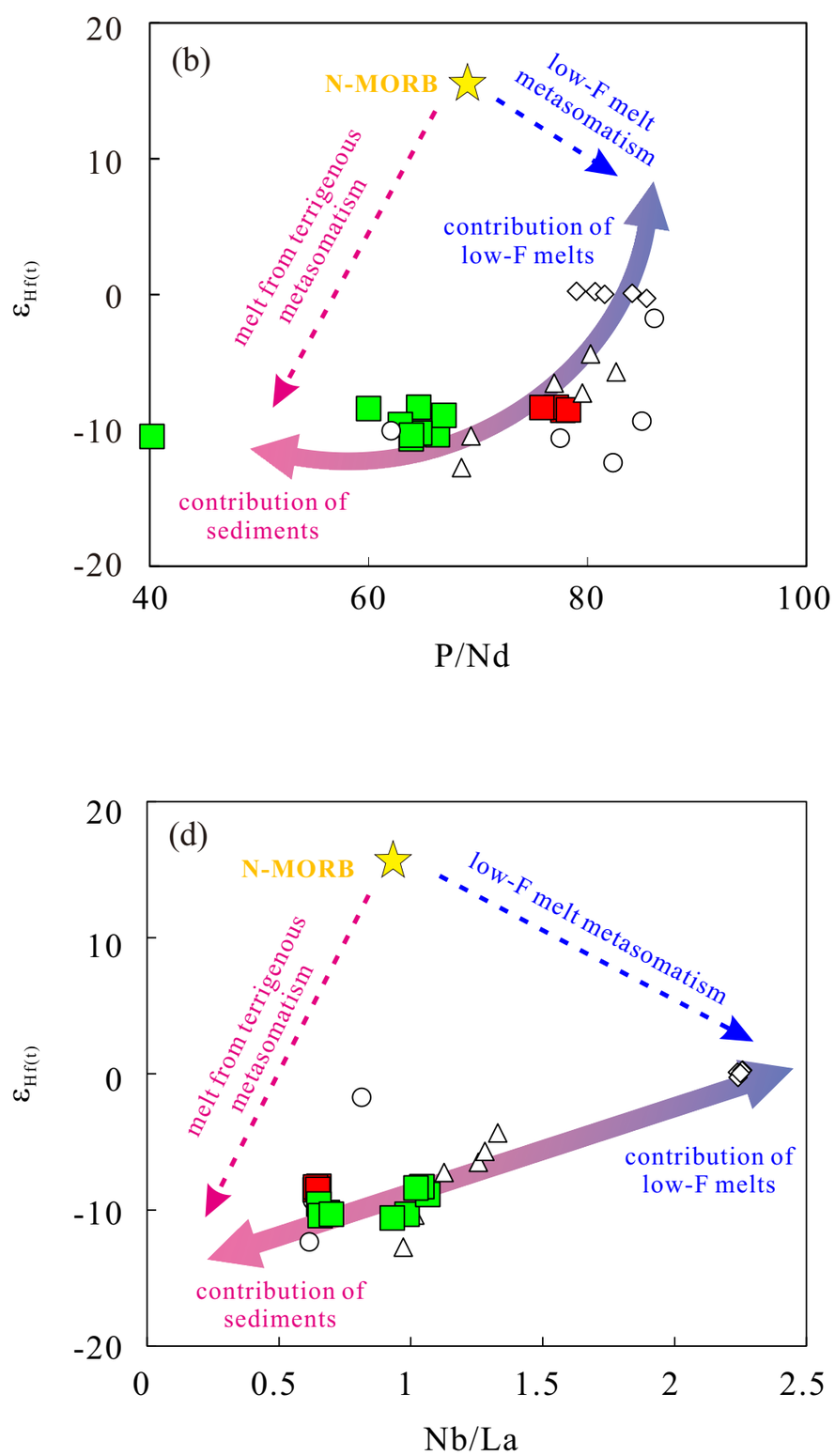
(b)
N-MORB
low-F melt metasomatism
melt from terrigenous metasomatism
contribution of low-F melts
contribution of sediments
$\varepsilon_{Hf(t)}$
P/Nd

(c)
N-MORB
low-F melt metasomatism
melt from terrigenous metasomatism
$\varepsilon_{Nd(t)}$
Nb/La

(d)
N-MORB
low-F melt metasomatism
melt from terrigenous metasomatism
contribution of low-F melts
contribution of sediments
$\varepsilon_{Hf(t)}$
Nb/La

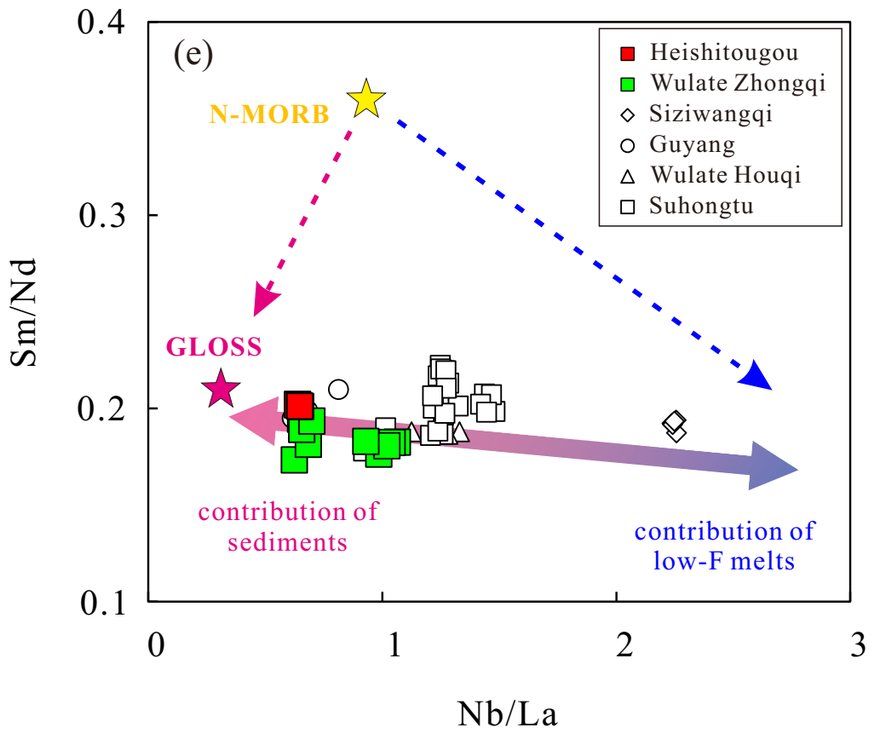
(e)
Heishitougou
Wulate Zhongqi
Siziwangqi
Guyang
Wulate Houqi
Suhongtu
N-MORB
GLOSS
contribution of sediments
contribution of low-F melts
Sm/Nd
Nb/La

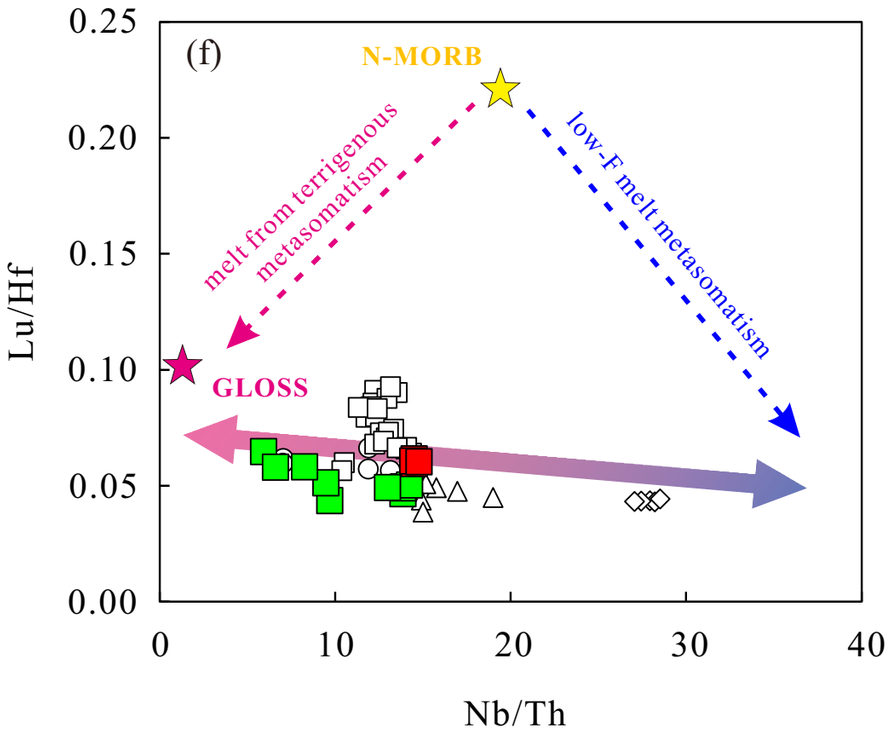
(f)
N-MORB
GLOSS
melt from terrigenous metasomatism
low-F melt metasomatism
Lu/Hf
Nb/Th

Fig. 9

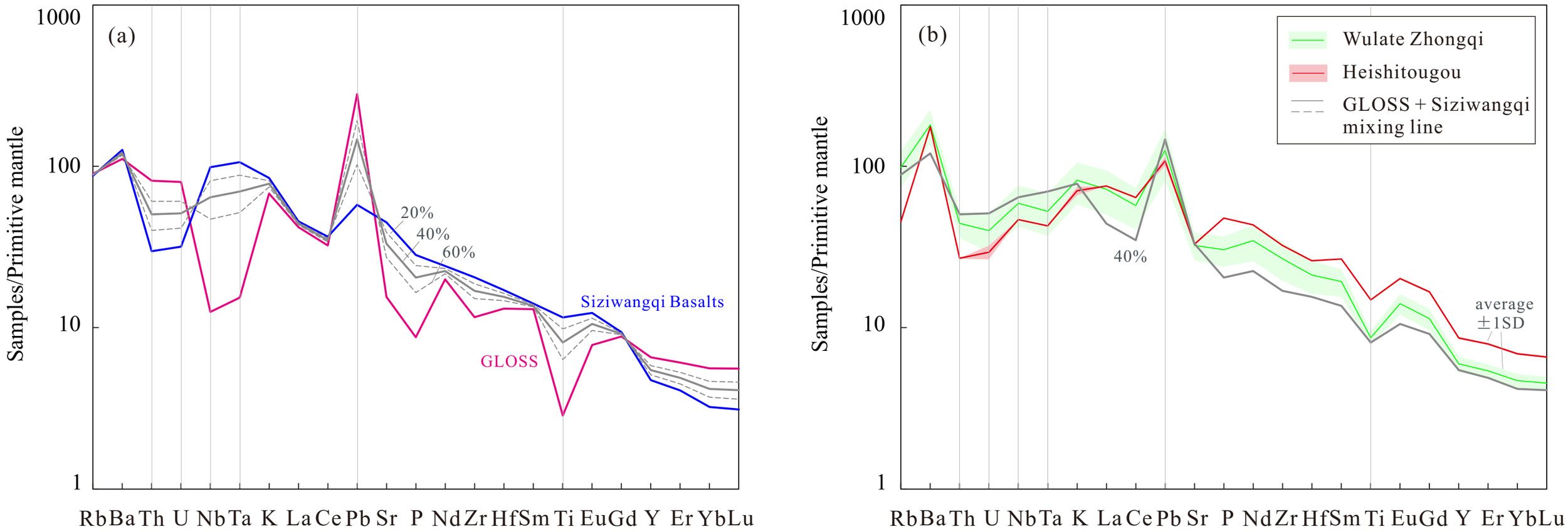
(a)
1000
100
10
1
Samples/Primitive mantle
20%
40%
60%
Siziwangqi Basalts
GLOSS
Rb Ba Th U Nb Ta K La Ce Pb Sr P Nd Zr Hf Sm Ti Eu Gd Y Er Yb Lu
(b)
Wulate Zhongqi
Heishitougou
GLOSS + Siziwangqi mixing line
40%
average
±1SD

Fig. 10

(a) >250Ma

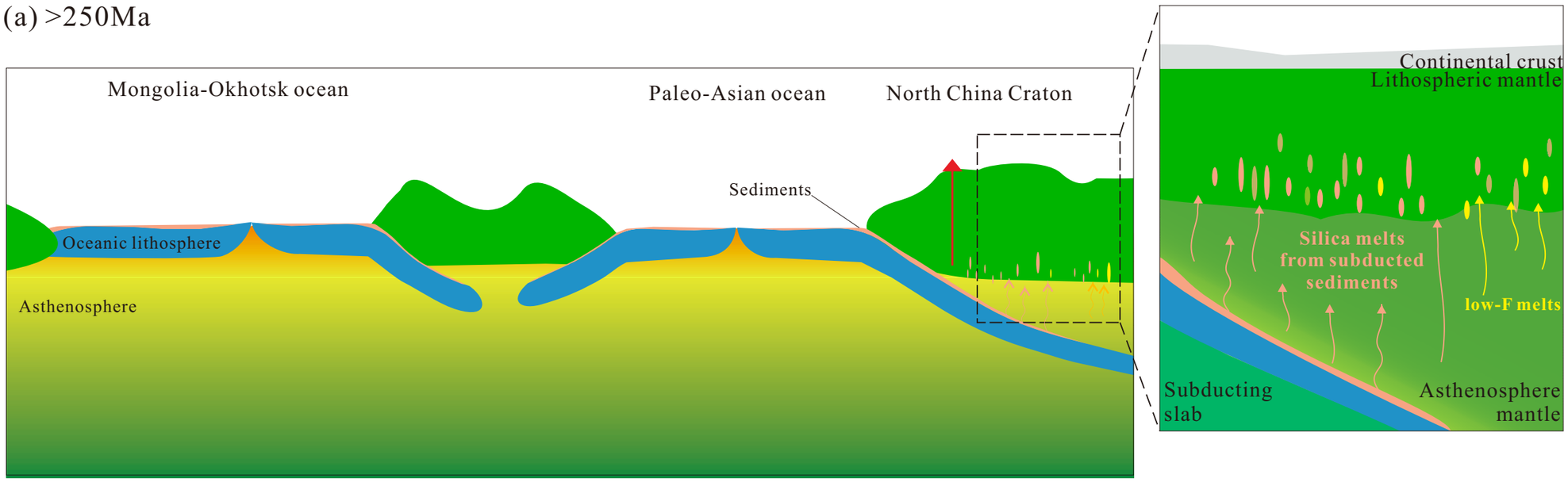

(b) Triassic ~ Middle Jurassic

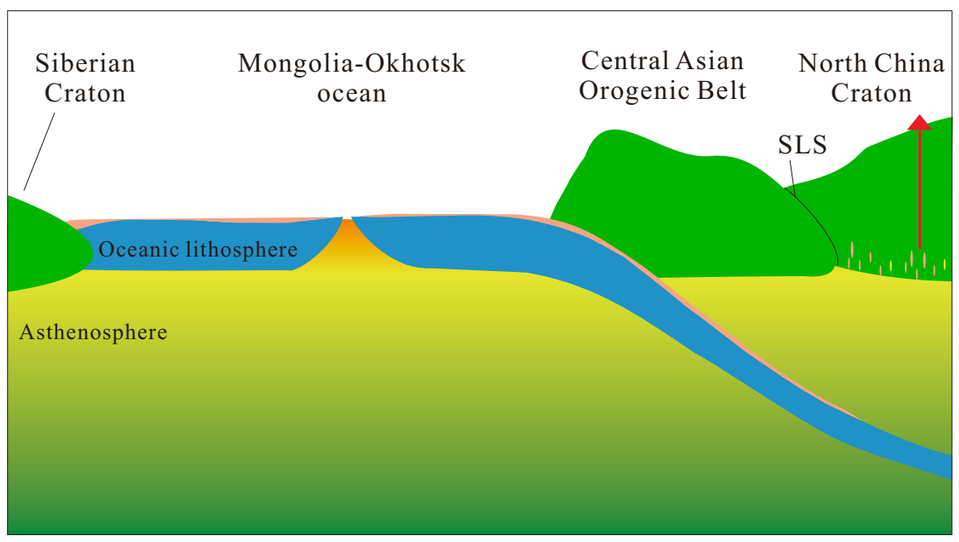

(c) Middle Jurassic

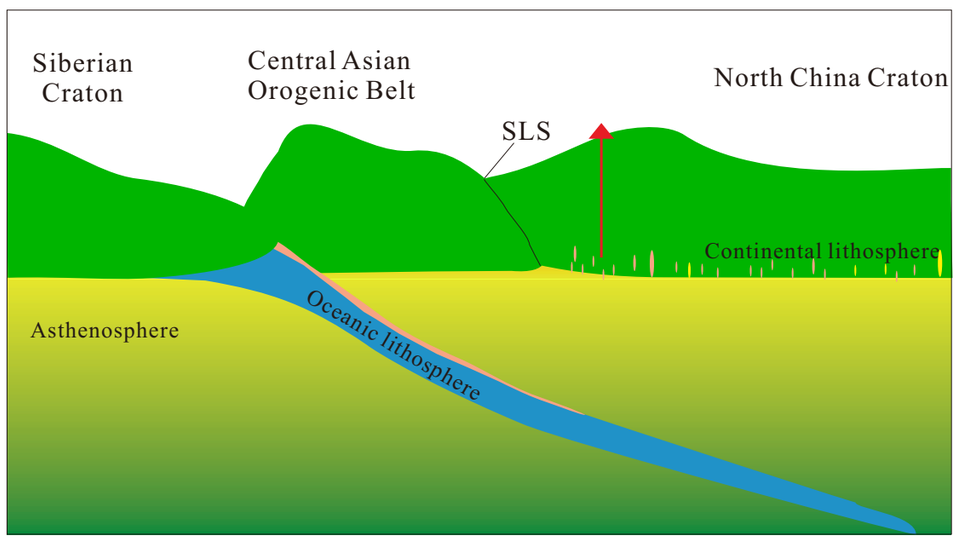

(d) ~120Ma

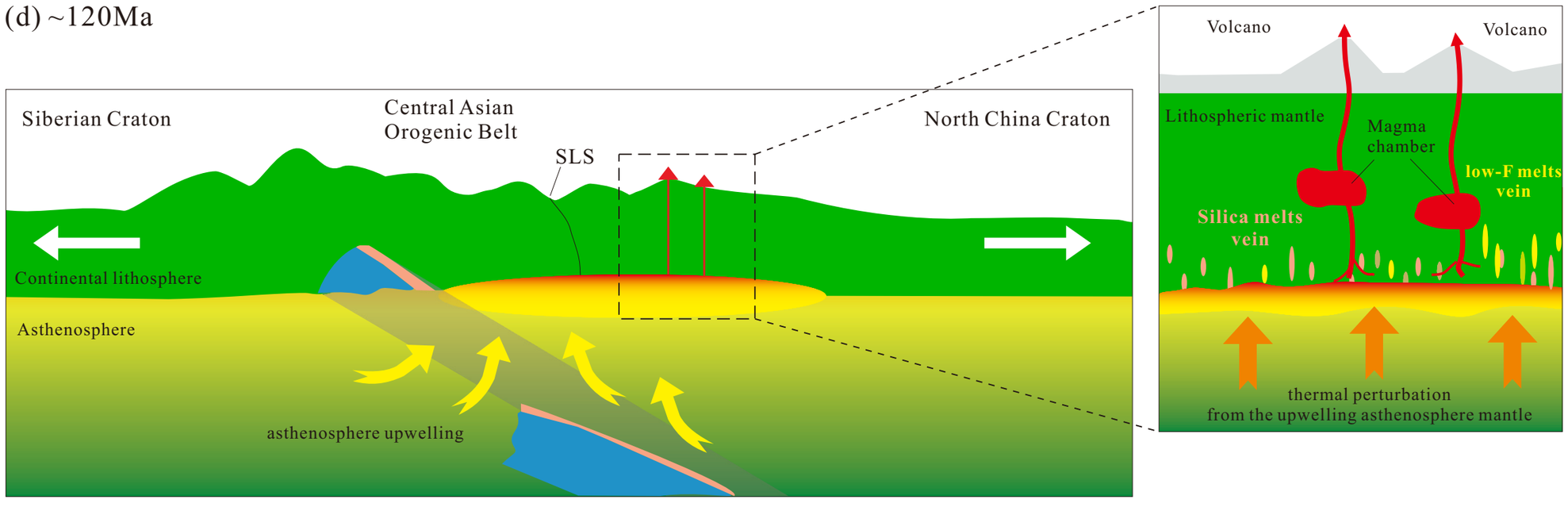

Table 1. Statistics of age data of early Cretaceous volcanics from the WNCC

Location	Rock type	Age（Ma）	Dating method	Data source
Siziwang Qi	Shoshonite	127 ± 2	Whole rock Ar-Ar	He et al., 2013
	Shoshonite	119.6 ± 1.4	Whole rock K-Ar	Zhang et al., 2005
	Shoshonite	128.4 ± 1.8	Whole rock K-Ar	
	Shoshonite	108.6 ± 1.4	Whole rock K-Ar	
Guyang	Basalt	133.13 ± 0.91	Whole rock Ar-Ar	Guo et al., 2018
	Basalt	123.47 ± 0.62	Whole rock Ar-Ar	
	Rhyolite	126.5 ± 1.3	SHRIMP zircon U-Pb	
	Rhyolite	126.1 ± 3.0	SHRIMP zircon U-Pb	
Wulate Zhongqi	Trachyte	122 ± 2	LA-ICP-MS Zircon U-Pb	Zhang, 2013
	Rhyolite	135 ± 2	LA-ICP-MS Zircon U-Pb	
	Basalt	116.35 ± 0.75	Whole rock Ar-Ar	This study
Wuchuan	Tuff	130 ± 3	LA-ICP-MS Zircon U-Pb	Zhang, 2013
Heishitougou	Basalt	126.2 ± 0.4	Whole rock Ar-Ar	Zou et al.,2008
Wulate Houqi	Basalt	114.42 ± 0.58	Whole rock Ar-Ar	Guo et al., 2018
	Basalt	107.30 ± 0.54	Whole rock Ar-Ar	
Suhongtu	Andesite to basalt	114.1 ± 0.3	Whole rock Ar-Ar	Zhu et al.，2008
	Andesite to basalt	113.8 ± 0.7	Whole rock Ar-Ar	
	Andesite to basalt	109.3 ± 2.8	Whole rock Ar-Ar	
	Andesite to basalt	110.8 ± 1.3	Whole rock Ar-Ar	
	Andesite to basalt	110.7 ± 1.6	Whole rock Ar-Ar	
	Andesite to basalt	110.3 ± 1.6	Whole rock Ar-Ar	
	Andesite to basalt	110.4 ± 1.2	Whole rock Ar-Ar	
	Andesite to basalt	110.9 ± 1.9	Whole rock Ar-Ar	
	Andesite to basalt	110.6 ± 1.5	Whole rock Ar-Ar	
	Andesite to basalt	111.1 ± 1.2	Whole rock Ar-Ar	
	Andesite to basalt	110.9 ± 2.3	Whole rock Ar-Ar	
	Alkali basalt	110.62 ± 1.40	Whole rock Ar-Ar	Zhong et al, 2015
	Alkali basalt	112.71 ± 2.06	Whole rock Ar-Ar	
	Alkali basalt	106.64 ± 1.38	Whole rock Ar-Ar	
	Alkali basalt	106.48 ± 1.32	Whole rock Ar-Ar	
	Alkali basalt	108.93 ± 1.68	Whole rock Ar-Ar	
	Alkali basalt	109.51 ± 1.76	Whole rock Ar-Ar	

Table 2. Bulk rock Sr-Nd-Hf isotope analysis result for the early Cretaceous basalts from Wulate Zhongqi and Heishitougou and the USGS standard materials

Sample	$^{87}Rb/^{86}Sr$ [a]	$^{87}Sr/^{86}Sr \pm 1\sigma$	$^{87}Sr/^{86}Sr_i$ [b]	$^{147}Sm/^{144}Nd$ [a]	$^{143}Nd/^{144}Nd \pm 1\sigma$	$^{143}Nd/^{144}Nd_i$ [b]	$^{176}Lu/^{177}Hf$ [a]	$^{176}Hf/^{177}Hf \pm 1\sigma$	$^{176}Hf/^{177}Hf_i$ [b]	$\varepsilon_{Nd(t)}$ [c]	$\varepsilon_{Hf(t)}$ [c]
ZQ14-04	0.284658	0.708013±8	0.707543	0.116999	0.512054±2	0.511965	0.009202	0.282452±4	0.282431	-10.22	-9.58
ZQ14-06	0.278009	0.707603±7	0.707143	0.113846	0.512042±4	0.511955	0.008238	0.282425±2	0.282407	-10.40	-10.44
ZQ14-09	0.191951	0.706930±3	0.706613	0.101585	0.511952±6	0.511875	0.005541	0.282325±1	0.282312	-11.97	-13.79
ZQ14-12	0.236677	0.707432±6	0.707040	0.116473	0.512043±3	0.511955	0.008261	0.282428±2	0.282410	-10.41	-10.34
ZQ14-26	0.164826	0.707251±5	0.706978	0.100089	0.511901±3	0.511825	0.005393	0.282231±1	0.282220	-12.94	-17.08
ZQ14-29	0.132837	0.707000±6	0.706780	0.106168	0.512261±6	0.512180	0.006623	0.282425±2	0.282410	-6.01	-10.33
ZQ14-37	0.300084	0.706725±4	0.706229	0.109955	0.512109±2	0.512025	0.007035	0.282466±1	0.282451	-9.04	-8.89
ZQ14-40	0.322481	0.706985±4	0.706452	0.109773	0.512130±2	0.512046	0.006978	0.282483±1	0.282468	-8.62	-8.30
ZQ14-44	0.341646	0.707099±5	0.706534	0.108778	0.512128±2	0.512045	0.007145	0.282480±1	0.282465	-8.64	-8.41
ZQ14-47	0.273976	0.707038±7	0.706585	0.110126	0.512036±3	0.511952	0.006982	0.282417±1	0.282402	-10.47	-10.62
ZQ14-52	0.299392	0.707984±5	0.707488	0.097399	0.511895±2	0.511821	0.005268	0.282223±2	0.282211	-13.02	-17.38
ZQ19-08	0.265713	0.707303±6	0.706864	0.105005	0.511984±2	0.511904	0.006247	0.282364±2	0.282351	-11.40	-12.43
ZQ19-12	0.218088	0.707262±5	0.706901	0.109203	0.512032±3	0.511948	0.007274	0.282430±2	0.282414	-10.53	-10.20
HSTG16-01	0.122298	0.706551±6	0.706331	0.121700	0.512108±4	0.512008	0.008737	0.282490±3	0.282455	-9.13	-8.53
HSTG16-02	0.123237	0.706641±8	0.706420	0.121044	0.512099±5	0.511999	0.008463	0.282482±3	0.282462	-9.31	-8.29
HSTG16-04	0.117542	0.706525±8	0.706314	0.121502	0.512098±4	0.511998	0.008607	0.282481±3	0.282461	-9.33	-8.33
HSTG16-09	0.119337	0.706525±8	0.706310	0.121104	0.512096±4	0.511996	0.008571	0.282476±3	0.282456	-9.35	-8.50
BHVO-2		0.703524±4			0.513012±3			0.283085±1			
BCR-2		0.705113±5			0.512655±4			0.282859±2			
AGV-2		0.704016±5			0.512797±4			0.282979±3			

a. $^{87}Rb/^{86}Sr$, $^{147}Sm/^{144}Nd$ and $^{176}Lu/^{177}Hf$ are calculated using whole-rock Rb, Sr, Sm, Nd, Lu and Hf contents in Supplementary Table 1.

b. $^{87}Sr/^{86}Sr_i = [(^{87}Sr/^{86}Sr) - (^{87}Rb/^{86}Sr)(e^{\lambda t}-1)]$; $^{143}Nd/^{144}Nd_i = [(^{143}Nd/^{144}Nd) - (^{143}Sm/^{144}Nd)(e^{\lambda t}-1)]$; $^{176}Hf/^{177}Hf_i = [(^{176}Hf/^{177}Hf) - (^{176}Lu/^{177}Hf)(e^{\lambda t}-1)]$.

c. $\varepsilon_{Nd(t)} = [(^{143}Nd/^{144}Nd_i)/(^{143}Nd/^{144}Nd_{CHURi})-1]\times 10000$, $^{143}Nd/^{144}Nd_{CHUR} = 0.512638$; $\varepsilon_{Hf(t)} = [(^{176}Hf/^{177}Hf_i)/(^{176}Hf/^{177}Hf_{CHURi})-1]\times 10000$; $^{176}Hf/^{177}Hf_{CHUR} = 0.282772$.

Supplementary Figure

Click here to access/download

Supplementary Interactive Plot Data (CSV)

Supplementary Tables.xlsx